Plectin-mediated cytoskeletal crosstalk as a target for inhibition of hepatocellular carcinoma growth and metastasis.

Zuzana Outla[1], Gizem Oyman-Eyrilmez[1], Katerina Korelova[1], Magdalena Prechova[1], Lukas Frick[2], Lenka Sarnova[1], Piyush Bisht[1], Petra Novotna[1], Jan Kosla[1,3], Patricia Bortel[4], Yasmin Borutzki[5], Andrea Bileck[4,6], Christopher Gerner[4,6], Mohammad Rahbari[3,7], Nuh Rahbari[8], Emrullah Birgin[8], Bibiana Kvasnicova[9], Andrea Galisova[10], Katerina Sulkova[10], Andreas Bauer[11], Njainday Jobe[12], Ondrej Tolde[12], Eva Sticova[13,14], Daniel Rosel[12], Tracy O'Connor[15], Martin Otahal[9], Daniel Jirak[10], Mathias Heikenwälder[3], Gerhard Wiche[16], Samuel M. Meier-Menches[4,5,6], Martin Gregor[1]

[1]Laboratory of Integrative Biology, Institute of Molecular Genetics of the Czech Academy of Sciences, Prague, Czech Republic

[2]Institute of Molecular Cancer Research, University of Zurich, Zurich, Switzerland

[3]Division of Chronic Inflammation and Cancer, German Cancer Research Center, Im Neuenheimer Feld 242, 69120, Heidelberg, Germany

[4]Department of Analytical Chemistry, University of Vienna, Waehringer Str. 38, 1090 Vienna, Austria

[5]Institute of Inorganic Chemistry, University of Vienna, Waehringer Str. 42, 1090 Vienna, Austria

[6]Joint Metabolome Facility, Medical University of Vienna and University of Vienna, Waehringer Str. 38, 1090 Vienna, Austria

[7]Department of Surgery, University Hospital Mannheim, Medical Faculty Mannheim, University of Heidelberg, Theodor-Kutzer-Ufer 1-3, 68167, Mannheim, Germany

[8]Department of General and Visceral Surgery, Ulm University Hospital, Ulm, Germany

[9]Department of Natural Sciences, Faculty of Biomedical Engineering, Czech Technical University in Prague, Kladno, Czech Republic

[10]Department of Radiodiagnostic and Interventional Radiology, Institute for Clinical and Experimental Medicine, Prague, Czech Republic

[11]Department of Physics, University of Erlangen-Nuremberg, Erlangen, Germany

[12]Department of Cell Biology, Faculty of Science, Charles University, BIOCEV, Prumyslova 595, 25242, Vestec, Czech Republic.

[13]Department of Clinical and Transplant Pathology, Institute for Clinical and Experimental Medicine, Prague, Czech Republic

[14]Department of Pathology, Third Faculty of Medicine, Charles University, Prague, Czech Republic

[15]Department of Biology, North Park University, Chicago, USA.

[16]Department of Biochemistry and Cell Biology, Max F. Perutz Laboratories, University of Vienna, Vienna, Austria

Correspondence to:

Martin Gregor, PhD

Laboratory of Integrative Biology, Institute of Molecular Genetics of the Czech Academy of Sciences

Videnska 1083, Prague 4, CZ-14220, Czech Republic

Phone: +420 241 063 461

Email: martin.gregor@img.cas.cz

Abstract

The most common primary malignancy of the liver, hepatocellular carcinoma (HCC), is a heterogeneous tumor entity with high metastatic potential and complex pathophysiology. Increasing evidence suggests that tissue mechanics plays a critical role in tumor onset and progression. Here we show that plectin, a major cytoskeletal crosslinker protein, plays a crucial role in mechanical homeostasis and mechanosensitive oncogenic signaling that drives hepatocarcinogenesis. Our expression analyses revealed elevated plectin levels in liver tumors, which correlated with poor prognosis for HCC patients. Using autochthonous and orthotopic mouse models we demonstrated that genetic and pharmacological inactivation of plectin potently suppressed the initiation and growth of HCC. Moreover, plectin targeting potently inhibited the invasion potential of human HCC cells and reduced their metastatic outgrowth in the lung. Proteomic and phosphoproteomic profiling linked plectin-dependent disruption of cytoskeletal networks to attenuation of oncogenic FAK, MAPK/Erk, and PI3K/AKT signatures. Importantly, by combining cell line-based and murine HCC models, we show that plectin inhibitor plecstatin-1 (PST) is well-tolerated and potently inhibits HCC progression. In conclusion, our study demonstrates that plectin-controlled cytoarchitecture is a key determinant of HCC development and suggests that pharmacologically induced disruption of mechanical homeostasis may represent a new therapeutic strategy for HCC treatment.

Introduction

Mounting evidence indicates that tissue mechanics plays a pivotal role in cancer cell and stromal cell behavior. Tumor progression is typically associated with a pathological increase of tissue stiffness caused by excessive deposition, crosslinking, and aberrant organization of dense extracellular matrix (ECM) fibers. Increasing tissue rigidity drives tumor invasion and malignancy and correlates with poor patient survival[1,2].

At the cellular level, both tumor and stromal cells respond to altered mechanical properties of the extracellular milieu by translating physical cues into mechanosensitive signaling pathways. This conversion relies on focal adhesions (FAs), clusters of integrin receptors facilitating the link between the ECM and the cytoskeleton. Integrin-mediated adhesion induces the activation of FAK, MAPK/Erk, and PI3K/AKT pathways, leading to increased cell survival, migration, and invasion[3-5]. Subsequent activation of Rho-dependent pathways results in higher cytoskeletal tension and force transmission across FAs, thus establishing a mechanical reciprocity between ECM viscoelasticity and actomyosin-generated cytoskeletal tension. Importantly, many genes encoding components of the ECM-cytoskeletal axis and their regulators (e.g. *αSMA*, *ITGβ*, *LMNA*, *ROCK*, and *COL*) are controlled by tension-dependent transcription[6,7]. This creates a difficult-to-break positive feedback loop leading to cellular and matrix stiffening, further promoting the aggressive, pro-proliferative, and invasive tumor cell phenotype.

Emerging therapeutic strategies aimed at tumor mechanics and mechanotransduction include the targeting of the ECM and ECM modulators (e.g. lysyl oxidase and angiotensin), depletion of stromal myofibroblasts, and integrin receptors[2,3]. Other approaches target cytoskeleton-mediated downstream cellular response to tissue stiffening (e.g. Rho-dependent actomyosin-generated contractile forces[8]). We hypothesized that another efficacious strategy could be inactivation of cytoskeletal crosslinker proteins (so-called cytolinkers)[9,10], large proteins of the plakin protein family, responsible for maintaining cellular architecture. The best-studied example, a prototypical cytolinker plectin is a well-established regulator of cellular tensional homeostasis and mechanotransduction[10] which is upregulated in various tumors[11,12]. Through its canonical actin-binding domain (ABD[13]) and intermediate filament (IF)-binding domain (IFBD[14]), plectin crosslinks actin with IF networks and recruits them to cell adhesions, including FAs. Plectin deletion or mutation results in cytoskeletal reconfiguration accompanied by altered mechanical properties, such as cellular stiffness, stress propagation, and traction force generation[15-18]. In addition, plectin-dependent changes in cell adhesions[18-21] and cytoskeletal tension[17,18,20-22] are associated with aberrant integrin-mediated mechanosignaling[20,21]. Although multiple reports have linked plectin with tumor malignancy[12] and

other pathologies[10,23], mechanistic insights into how plectin functionally contributes to carcinogenesis remain largely unknown.

A malignancy with a well-known link to overproduction of ECM components is hepatocellular carcinoma (HCC), the most common type of liver cancer. Repeated rounds of hepatocyte damage and renewal due to a number of etiologies, most commonly chronic viral infection, alcohol abuse, or a diet rich in fats and sugars, creates a pro-inflammatory environment in the liver. Activated hepatic stellate cells adopt a myofibroblast phenotype and increase production and deposition of ECM components leading to liver fibrosis which can eventually progress to liver cirrhosis. Up to 90% of HCC cases occur on a background of liver fibrosis or cirrhosis, suggesting a causal link between increased deposition of ECM components and liver carcinogenesis. Consistent with this idea, plectin mRNA has been found to be upregulated in liver carcinomas, especially in later stages of disease[11]. Thus, changes in the interactions between the cytoskeleton and ECM may be important in HCC progression, particularly during the transition from local to metastatic malignancy.

Here we explore the role of plectin in the development and dissemination of HCC. Using publicly available HCC sequencing data and biopsies from HCC patients we identify plectin as a novel HCC marker associated with a malignant phenotype and poor survival. To explore the role of plectin in hepatocarcinogenesis, we use a genetic mouse model with liver-specific plectin ablation ($Ple^{\Delta Alb}$). In this model, plectin deficiency suppresses tumor initiation and growth. We further demonstrate that CRISPR/Cas9-engineered human HCC cell lines with inactivated plectin display limited migration, invasion, and anchorage-independent proliferation which correlates with their reduced metastatic outgrowth in the lung. By comprehensive proteomic analysis, we show that plectin inactivation attenuates oncogenic FAK, MAPK/Erk, and PI3K/AKT signaling signatures. Finally, our work identifies the ruthenium-based plecstatin-1 (PST), as a candidate drug that can mimic the genetic ablation of plectin, thus providing a robust pre-clinical proof-of-concept for PST in the treatment of HCC. Our study implicates plectin as a potent driver of HCC, highlights its importance in metastatic spread, and points to potential novel treatment options.

Results

Plectin levels are elevated in HCC and predict a poor prognosis

Using 17 distinct HCC patient datasets, we confirmed that *plectin* expression is consistently and significantly increased in HCC samples when compared to non-tumor (NT) liver tissues (Fig. 1A). The analysis of data from The Cancer Genome Atlas (TCGA) confirmed elevated *plectin* expression in HCC, irrespective of HCC etiology or gender (Figure 1—figure supplement 1A-D). To assess whether high plectin expression is typical for a specific subpopulation of HCC patients, we created t-SNE plots and compared plectin expression patterns with those of molecular subclasses of Dr. Chang´s and Dr. Boyault´s classification[24,25]. Although we observed local clusters of patients with higher or lower plectin expression levels, they did not seem to be associated with any of the largest clusters or subgroups (Figure 1—figure supplement 1E). Strikingly, using higher tertile expression as the cut-off, higher *plectin* mRNA levels were associated with a significant decrease in recurrence-free survival (Fig. 1B). A similar trend was observed across 8 distinct HCC datasets (Figure 1—figure supplement 1F).

Consistent with expression analysis, quantitative immunofluorescence microscopy of 19 human HCC tissue sections revealed a significant increase of plectin fluorescence intensities in tumor (T) compared to adjacent non-tumor (NT) tissue, with plectin perimembraneous enrichment in tumor hepatocytes (Fig. 1C; Figure 1—figure supplement 1G). Next, we compared plectin expression levels by immunoblotting in a panel of human HCC cell lines, which represent distinct stages of HCC development[24]. Consistent with mRNA and immunofluorescence analyses, poorly differentiated mesenchymal-like HCC cell lines (characterized by low E-cadherin and high vimentin levels) displayed elevated plectin levels, coinciding with higher migration speed when compared to well-differentiated HCC cell lines (Fig. 1D,E).

To validate our findings in a well-established chemical carcinogen murine HCC model, we analyzed plectin expression in hepatic tumors formed 46 weeks after diethylnitrosamine (DEN) injection in C57Bl/6J mice (Fig. 1F). Both quantitative immunofluorescence and immunoblot analyses indicated elevated plectin levels in T versus NT liver tissue (Fig. 1C,G,H; Figure 1—figure supplement 1H). Moreover, enhanced plectin signal along hepatocyte membranes closely resembled the staining pattern found in patient HCC sections (Fig. 1C), suggesting reliable translation from the human setting. Together, these results show that elevated plectin is associated with HCC progression both in human patients and animal model and indicates robust prognostic potential for patient survival.

Plectin promotes hepatocarcinogenesis

To determine the functional consequences of plectin loss in liver tumor development, we analyzed the formation of DEN-induced HCCs in mice lacking plectin expression in the liver using magnetic resonance imaging (MRI). To achieve liver-specific plectin deletion, mice carrying a floxed plectin sequence (*Ple*$^{fl/fl}$) were crossed to mice expressing the Cre recombinase under the liver-specific albumin promoter (*Alb-Cre*). The resulting mice (*Ple*$^{\Delta Alb}$) lack plectin expression in the liver[26]. Remarkably, MRI screening 32 and 44 weeks post-injection revealed a significant reduction of tumor number and volume in *Ple*$^{\Delta Alb}$ mice compared to *Ple*$^{fl/fl}$ controls (Fig. 2A-C). Decreased tumor burden in the second cohort of *Ple*$^{\Delta Alb}$ mice was confirmed macroscopically 44 weeks after DEN administration (Fig. 2D,E). Notably, *Ple*$^{\Delta Alb}$ mice more frequently formed larger tumors, as reflected by overall tumor size increase (Fig. 2F; Figure 2—figure supplement 1A), possibly implying reduced migration or increased cohesion of plectin-depleted cells[26,27].

To address plectin´s role in HCC at a cellular level, we genetically manipulated endogenous plectin in well-differentiated Huh7 and poorly differentiated SNU-475 human HCC cell lines[24]. Using the CRISPR/Cas-9 system we generated either knockouts (KO) or cells harboring endogenous plectin with deletion of the IF-binding domain (ΔIFBD) as functional knockouts[18] (Figure 2—figure supplement 1B-D). Gene editing was complemented by treatment with organoruthenium-based compound PST that inactivates plectin function[18,28]. If not stated otherwise, we applied PST in the final concentration of 8 µM, which corresponds to the 25% of IC_{50} for Huh7 cells (Figure 2—figure supplement 1E). Consistent with the murine model, plectin inactivation resulted in a reduced number of Huh7 and SNU-475 colonies in a soft agar colony formation assay, with PST treatment closely mimicking the effect of genetic targeting (Fig. 2G). Moreover, KO and ΔIFBD SNU-475 colonies were significantly smaller when compared to wild-type (WT) controls, with a similar trend observed for Huh7 cells (Figure 2—figure supplement 1F). Collectively, these data demonstrate the inhibitory effect of plectin inactivation on HCC progression in adhesion-independent conditions.

To further assess whether plectin is required for human HCC progression, we investigated the growth of subcutaneous Huh7 xenografts in immunodeficient NSG mice (Fig. 2H; Figure 2—figure supplement 1G). Cells with disabled plectin developed significantly smaller tumors when compared with untreated WT cells (Fig. 2H), mirroring the results of the colony forming assay. The percentage of $Ki67^+$ cells on immunolabeled xenograft sections, however, did not differ between experimental conditions (Figure 2—figure supplement 1G). These results show the reduced tumorigenic potential of human HCC cells when plectin is disabled either by CRISPR/Cas9-mediated gene ablation or

pharmacologically with PST. Hence, by combining *in vivo* and *in vitro* approaches, we provide evidence that plectin promotes hepatocarcinogenesis.

Plectin controls oncogenic FAK, MAPK/Erk, and PI3K/Akt signaling in HCC cells

To identify potential molecular effectors and signaling pathways mediating the tumor suppressive effects of plectin inactivation, we profiled the proteomes of WT, KO, and PST-treated WT SNU-475 cells using MS-based shotgun proteomics and phosphoproteomics (Fig. 3A-C; Figure 3—figure supplement 1A,B). Using a label free quantification strategy, a total of 5440 protein groups and 3573 phosphosites were detected. We found 265 protein groups significantly regulated (FDR < 0.05; s0 = 0.01) upon plectin ablation when comparing WT and KO SNU-475 proteomes (Fig. 3B). Ingenuity Pathway Analysis (IPA) revealed major plectin-dependent regulation of signaling pathways related to the actin cytoskeleton, such as “RhoA signaling”, “Actin cytoskeleton signaling”, “Integrin signaling”, and “Signaling by Rho family GTPases” (Fig. 3B). Similarly, 313 regulated phosphosites indicated a major impact on actin, as well as “ILK signaling”, “FAK signaling”, and “Molecular mechanisms of cancer” among the most altered pathways (Fig. 3B).

Analysis of proteome differences between WT and PST-treated cells identified abundance changes (FDR < 0.05; s0 = 0.01) in 1178 proteins and 290 phosphoproteins (Fig. 3C). A comparison of KO and PST signatures using IPA revealed an overlap (Figure 3—figure supplement 1A). Consistently, the IPA annotation linked also PST signature to integrin- and cytoskeleton-related signaling pathways such as “ILK signaling”, “Integrin signaling”, “RhoA signaling”, and “Actin cytoskeleton signaling” (Fig. 3C). Taken together, our proteomic analyses suggest a regulatory role for plectin in the mechanosensitive, cell adhesion-linked signaling which is critical for cancer development and dissemination[3-5].

To independently confirm our MS findings, we performed extensive immunoblot analysis of WT, KO, ΔIFBD, and PST-treated Huh7 and SNU-475 cells with a focus on integrin-associated adhesome network (Fig. 3D; Figure 3—figure supplement 1C). In agreement with our proteomic analyses, plectin inactivation resulted in considerable changes in expression levels of integrin adhesion receptors (integrins αV and β1) as well as other FA constituents (i.e. talin, vinculin, and paxillin). Moreover, immunoblotting revealed in cells with disabled plectin either generally altered expression (FAK, AKT, Erk1/2, ILK, and PI3K) and/or reduced phosphorylation (AKT, Erk1/2, and PI3K) of key effectors downstream of integrin-mediated adhesion. Although these alterations were not found systematically in both cell lines and condition (reflecting thus presumably their distinct differentiation grade and

plectin inactivation efficacy), collectively these data confirmed plectin-dependent adhesome remodeling together with attenuation of oncogenic FAK, MAPK/Erk, and PI3K/Akt pathways upon plectin inactivation (Fig. 3E).

Plectin-dependent disruption of cytoarchitecture accounts for hampered migration of HCC cells

As plectin acts as a major organizer of cytoskeletal networks[10], we next investigated cytoskeletal organization in HCC cells by immunofluorescence microscopy. To circumvent considerable variability in cellular morphology, which largely obscures quantitative assessment of cytoarchitecture, we seeded WT, KO, ΔIFBD, and PST-treated SNU-475 cells on crossbow-shaped micropatterns[29]. Reminiscent of plectin-deficient fibroblasts[20,30], plectin inactivation in SNU-475 cells produced less delicate vimentin networks compared to WT cells, with filaments often bundled and sometimes collapsing into vimentin clumps (Fig. 4A,B). A quantitative analysis revealed uneven distribution of vimentin filaments throughout the cytoplasm of KO, ΔIFBD, and PST-treated WT cells as evidenced by the distance between the position of the center of vimentin intensity mass and the cell center (Figure 4—figure supplement 1A-C). In addition to the aberrant vimentin phenotype, we noticed a dramatic reduction in longitudinal dorsal actin stress fibers and transversal arcs, as well as pronounced ventral stress fibers in plectin-disabled cells (Fig. 4A,C,D). Moreover, we detected a reduction in F-actin fluorescence intensity in both Huh7 and SNU-475 KO cells, as well as a decrease of atomic force microscopy (AFM)-inferred cellular stiffness as a functional readout for a well-formed cytoskeleton[16] (Figure 4—figure supplement 1D-G).

Given the extent of plectin-dependent adhesome remodeling (Fig. 3D,E; Figure 3—figure supplement 1C), we next assessed whether plectin inactivation affects the morphology and localization of FAs in vinculin-immunolabeled SNU-475 cells. Remarkably, while FAs of micropattern-seeded WT cells were mostly located at the cell periphery, FAs of plectin-disabled cells were frequently found within the cell interior (Fig. 4A,E). Moreover, plectin inactivation resulted in an overall reduced number of FAs, and the FAs that remained were larger and more elongated than in WT cells (Fig. 4F,G; Figure 4—figure supplement 1H,I). To test whether the changes in actin/FA configuration affected adhesion-transmitted forces, we performed traction force microscopy (TFM; Fig. 4H,I). The smaller FAs found in WT cells transmitted significantly higher contractile energy than KO, ΔIFBD, and PST-treated cells, indicating that FAs in plectin-deficient cells were less functional than in WT.

Functional transmission of actomyosin-generated forces across FAs constitutes a prerequisite for cellular locomotion[31]. Therefore, we examined the effect of plectin inactivation on the migration of HCC cells. As anticipated, both Huh7 and SNU-475 cells exhibited a decrease in migration speed upon plectin targeting in the scratch wound healing assay (Fig. 5A,B; Figure 5—figure supplement 1A). It is noteworthy that migrating plectin-disabled SNU-475 cells exhibited more cohesive, epithelial-like features while progressing collectively. By contrast, WT SNU-475 leader cells were more polarized and found to migrate into scratch areas more frequently than their plectin-deficient counterparts (Figure 5—figure supplement 1B). Consistent with this observation, individually seeded SNU-475 cells less frequently assumed a polarized, mesenchymal-like shape upon plectin inactivation in both 2D and 3D environments (Fig. 5C). Moreover, plectin-inactivated SNU-475 cells exhibited a decrease in N-cadherin and vimentin levels when compared to WT counterparts (Figure 5—figure supplement 1C).

In addition to slower general migration, we also found epithelial growth factor (EGF)-guided migration potential of individual KO, ΔIFBD, and PST-treated cells to be significantly reduced compared to WT cells. Consistent with previous findings[20], plectin-disabled cells traversed less linear trajectories in both random and directed scenarios (Fig. 5D,E; Figure 5—figure supplement 1D,E). To determine whether plectin is involved in migration-associated cellular shape dynamics, we further investigated protrusions of SNU-475 cells using morphodynamic contour analysis[32]. Our analysis revealed a higher protrusion frequency of randomly migrating WT compared to plectin-disabled cells (Figure 5—figure supplement 1F), while no differences in protrusion orientation were observed (Fig. 5F-H). In sharp contrast, plectin ablation dramatically reduced the capacity of KO and ΔIFBD cells to form stable protrusions in the direction of chemotactic motion (Fig. 5F-H), although only a marginal effect on the protrusivity was observed (Figure 5—figure supplement 1F). Collectively, these results show that plectin is essential for the proper cytoskeletal configuration of HCC cells and their cytoskeleton-linked FAs. Moreover, they provide evidence that aberrant cytoarchitecture of plectin-disabled cells accounts for the failure to effectively exert traction forces and actively reconfigure body shape, both of which are required for HCC cell migration.

Plectin inactivation reduces HCC cell invasion and lung colonization

To investigate whether disruption of cytoarchitecture in plectin-disabled HCC cells also affected 3D migratory behavior, we compared the activity of WT, KO, ΔIFBD, and PST-treated SNU-475 cells in transwell and spheroid invasion assays. In both assays, plectin inactivation significantly reduced invasion potential compared to WT cells (Fig. 6A-C; Figure 6—figure supplement 1A). Unexpectedly,

plectin-targeted cells also degraded dramatically less FITC-labeled gelatin, suggesting that slower invasion is accompanied by defects in ECM degradation (Fig. 6D; Figure 6—figure supplement 1B).

To monitor plectin effects on shape dynamics in a 3D environment, we recorded WT and KO SNU-475 cells by time-lapse video microscopy in a matrigel invasion assay. Invading WT cells exhibited polarized protrusions followed by cell body displacement in the direction of the nascent protrusion (Video 1; Fig. 6E). By contrast, randomly oriented thinner protrusions of KO cells were often retracted shortly after formation. Markedly thinner and branched KO protrusions were confirmed by subsequent immunofluorescence microscopy (Fig. 6E). Similar to what we observed in the 2D assay, KO cells failed to invade in the direction of these transient protrusions (Video 1; Fig. 6E). Hence, plectin-controlled cytoarchitecture facilitates both 2D and 3D HCC cell migration.

Tumor, node, metastasis (TNM) classification of an HCC meta-cohort with clinically annotated tumors from HCC patients (n = 978) demonstrated that high plectin mRNA expression is associated with advanced TNM stages (Fig. 6F). To elucidate the impact of plectin inactivation on HCC dissemination, we conducted the lung colonization assay using both Huh7 and SNU-475 cells (Fig. 6G-I; Figure 6—figure supplement 1C-F). To this end, we administered red firefly luciferase and GFP (RedFLuc-GFP)-expressing WT and KO cells intravenously (i.v.) in 5-week-old NSG mice. Whereas mice receiving WT Huh7 (but not SNU-475; data not shown) cells succumbed rapidly to disease, mice receiving KO cells exhibited prolonged survival (Fig. 6G). To identify early phase of metastasis formation, we next monitored the HCC cell retention in the lungs using *in vivo* bioluminescence imaging (Fig. 6H). This experimental cohort was expanded for WT-injected mice which were administered PST two times a day for 5 weeks (WT+PST). Mice were sacrificed 5 weeks post-injection when the first luminescence-positive chest areas were detected (Fig. 6H) and cleared whole lung lobes were analyzed by lattice light sheet fluorescence microscopy (Fig. 6I). Although no macroscopic Huh7 nodules were visible, we found a prominent reduction in the number and volume of GFP-positive KO- and WT+PST-derived metastatic nodules. Thus, both CRISPR/Cas9-based and pharmacological plectin inactivation in HCC potently inhibits metastatic load in the lungs, identifying plectin as a potential target against tumor dissemination *in vivo*.

Genetic and pharmacological plectin targeting prevents hepatocarcinogenesis through signatures shared by animal models and patients

To further investigate the translational potential of PST treatment, we evaluated the effects of PST administration on hepatocarcinogenesis in additional murine model. To this end, we induced

multifocal HCC tumors by hydrodynamic delivery of a *c-myc* (Myc)-encoding element together with a CRISPR/Cas9 construct targeting *Tp53* (sgTp53)[33]. To test whether HCC onset and progression are sensitive to pharmacological targeting of plectin, we monitored Myc;sgTp53-driven tumor development in $Ple^{fl/fl}$, $Ple^{\Delta Alb}$, and PST-treated $Ple^{fl/fl}$ male mice using MRI (Fig. 7A). Consistent with our *in vitro* observations, MRI analysis at 4, 6, and 9 weeks post-induction revealed that both genetic and pharmacological plectin inactivation results in a substantial reduction in the average tumor number per mouse and the tumor incidence (Fig. 7A). Stalled development of $Ple^{\Delta Alb}$ and PST-treated $Ple^{fl/fl}$ tumors was also reflected by a decrease in liver/body weight ratio in another male cohort sacrificed at 6 weeks post-induction (Fig. 7B,C). The quantitative immunofluorescence microscopy revealed comparable rates of proliferation and apoptosis in Myc;sgTp53-induced tumors across experimental conditions (Figure 7 —figure supplement 1A,B). Comparable trends in liver/body weight ratio and tumor incidence were also found in a female cohort sacrificed 8 weeks post-induction (Figure 7—figure supplement 1C,D).

To better understand the antitumor effects observed in PST-treated mice, we performed proteomics on Myc;sgTp53-treated $Ple^{fl/fl}$, $Ple^{\Delta Alb}$, and PST-treated $Ple^{fl/fl}$ livers. Consistent with (phospho)proteomic and immunoblot analyses of HCC cell lines (Fig. 3A-E) we found a high level of similarity between $Ple^{\Delta Alb}$ and PST-treated $Ple^{fl/fl}$ signatures (Fig. 7D; Figure 7—figure supplement 2A,B). In addition, gene set enrichment analysis (GSEA)[34] revealed enrichment in “PI3K/Akt” or “Hippo/YAP signaling” pathways (Fig. 7D). Although the data from liver tissue proteomics showed some degree of variation, enrichment of tension-dependent signatures points toward similar trends found in *in vitro* scenarios. To further translate our findings to the human setting, we correlated plectin transcript levels with differentially expressed signatures identified in proteomic analysis of HCC cells (Fig. 3B-D). Through analysis of 1268 HCC patients, we found gene sets annotated as “Integrin pathway”, “FAK pathway”, “PI3K Akt/mTOR signaling” or “Erk pathway” to positively correlate with elevated plectin expression (Fig. 7E; Figure 7—figure supplement 2C; Figure 7—figure supplement 3). Collectively, these data connect plectin with well-characterized pro-oncogenic signaling pathways which were previously identified as prime candidates for therapeutic intervention in cancer[3-5].

Discussion

HCC represents a leading cause of cancer-related death, characterized by poor long-term prognosis, high postoperative recurrence, and a high rate of metastasis[35,36]. As chemotherapy, surgical resection, radiation, and local ablation are not effective in a large group of patients[35,37], there is an urgent need to develop effective therapeutic strategies to target HCC. By combining comprehensive analysis of CRISPR/Cas9-engineered HCC cell lines with (phospho)proteomics, mouse modeling as well as human patient data, we identified the plakin family member plectin as a novel HCC marker and druggable target upstream of FAK, MAPK/Erk, and PI3K/AKT signaling. Thus, our data link plectin, a cytolinker implicated in cytoskeletal tension and mechanotransduction with a major oncogenic signaling hub controlling growth and metastasis of HCC.

We began this work by assessing plectin expression in publicly available HCC patient datasets. Our meta-analyses revealed plectin transcript levels to be considerably elevated in HCC irrespective of etiology or gender, whereas previous findings in HCC were inconsistent[11,38]. Notably, we found that patients with higher *PLEC* mRNA levels had significantly shorter recurrence-free survival times than those with lower *PLEC* mRNA levels. Strikingly, *PLEC* expression in publicly available datasets was significantly associated with gene signatures related to „cell survival and proliferation“, „angiogenesis“, and „hypoxia“ (Figure 7—figure supplement 3) indicating that the *PLEC* level was associated with more aggressive cancer traits in HCC patients. In addition, plectin expression levels were associated with TNM staging, underscoring plectin´s prognostic value for HCC patient survival. Although HCC transcriptomes appears to differ from other cancers[39], our findings are in line with higher *PLEC* expression in other cancer entities such as oral squamous cell carcinoma[40,41], testicular cancer[42], or pancreatic cancer[43], and identify plectin as a specific marker for both early and advanced stages of HCC.

We and others have proposed that plectin plays a central role in tumor growth and dissemination[12,44]. Here, using liver-specific $Ple^{\Delta Alb}$ knockout mice[26], we show that plectin ablation in hepatocytes significantly reduced tumor burden in a model of DEN-induced HCC[45], which mimics fundamental aspects of human disease[46]. These mice also showed decreased hepatocarcinogenesis in a powerful model of multifocal HCC formation following hydrodynamic delivery of Myc;sgTp53[33,47]. In this model, both genetic and PST-mediated pharmacological inactivation of plectin not only reduced the number of HCC tumors formed but ultimately resulted in significantly improved survival of $Ple^{\Delta Alb}$ female mice. Complementing the data from both HCC models, we found that plectin inactivation resulted in the reduced tumorigenic potential of human HCC cells, as evidenced by reduced colony growth under adhesion-independent conditions or subcutaneous xenografts in immunodeficient NSG

mice. While several approaches (such as genetic manipulation[48], PST treatment[28] or blocking peptides[49] and antibodies[50]) decreasing the levels of functional plectin also lead to limited xenograft growth, to our knowledge, this is the first study showing that plectin inactivation prevents tumor progression in well-established preclinical mouse models.

Our previous studies demonstrated that plectin inactivation abrogates physical crosstalk between actin and IF networks[18,20], leading to the redistribution of internal tension[18], and ultimately resulting in defects in cell adhesions[20]. Indeed, plectin-dependent cytoskeletal disruption and aberrant adhesions have been previously linked to compromised migration and invasion of many non-cancerous[19,20,22,51,52] as well as cancerous cell types[48,53-56], including HCC cells[27]. In support of this concept, we report the collapse of actin and vimentin IF networks in Huh7 and SNU-475 cells with disabled plectin. Cytoskeletal disruption was accompanied by redistribution of misshapen FAs, which exerted reduced traction forces onto the underlying substrates. As anticipated, aberrant cytoarchitecture resulted in significantly slower motility of HCC cells in both 2D and 3D environments. Consistent with *in vitro* findings, plectin inactivation reduced metastatic outgrowth of HCC cells in the lung. Intriguingly, morphodynamic contour analysis revealed in these cells reduced capacity to form stable protrusions implicated in driving path finding and cellular locomotion[31]. Collectively, our data suggest that plectin is essential for spatiotemporal cytoskeletal rearrangement, cell shape stabilization, and effective transmission of traction forces, and place plectin-mediated cytoskeletal crosstalk at the center of the processes that control the metastatic cascade.

Plectin-mediated cytoskeletal crosstalk at FAs facilitates their essential features such as dynamics[20], adhesion strength[57], and mechanotransduction capacity[20]. Loss of vimentin filament-FA linkage upon plectin deletion in highly migratory dermal fibroblasts was shown to uncouple the activation of FAK from actomyosin-generated tension and attenuate downstream effectors such as Src, Erk1/2, and p38[20]. Here we show that plectin-dependent perturbation of the cytoskeleton-FAs interplay in invasive SNU-475 HCC cells profoundly altered (phospho)proteomic signatures of cytoskeleton- and cell adhesion-annotated proteins, thereby modulating mechanosensitive integrin-associated signaling events. Importantly, our (phospho)proteomic and immunoblot analyses identified attenuated signaling along FAK, MAPK/Erk, and PI3K/Akt axes as a consequence of plectin inactivation in both Huh7 and SNU-475 HCC cells. Plectin´s control of cytoskeletal crosstalk and its interplay with pro-oncogenic signaling pathways thus emerges as a critical determinant of the initiation and progression of HCC. It is noteworthy that plectin-dependent effects on PI3K/Akt and FAK/Erk signaling were recently described for prostate cancer[53,56] and head and neck squamous carcinoma cells[58], indicating that these observations have broader implications beyond liver cancer.

Finally, we were able to translate our findings from HCC cell lines and mouse models to HCC patients. By mining data from a large human patient cohort, we found a positive correlation between plectin expression and FA-associated FAK, Erk, and PI3K/Akt pathway gene sets. However, it is conceivable that dysregulated cytoskeletal crosstalk could affect HCC through multiple mechanisms independent from FA-associated signaling. Indeed, we and others[26,27] have shown that upon plectin inactivation, liver cells acquire epithelial characteristics that promote increased intercellular cohesion and reduced migration. Further studies will be required to identify and investigate synergistic adhesion-independent effects of plectin inactivation on HCC growth and metastasis.

Current systemic therapies for advanced HCC rely on a combination of multikinase inhibitors (such as sorafenib) or anti-VEGF /VEGF inhibitor (such as bevacizumab) treatment with immunotherapy[59]. Multikinase inhibitors provide only moderate survival benefit[60,61] due to primary resistance and the plasticity of signaling networks[62], and only a subset of patients benefits from addition of immunotherapy in HCC treatment[63]. Therefore, the most translationally impactful finding of this work is the ability of a small organoruthenium compound PST, a high-affinity plectin ligand, to effectivelly limit hepatocarcinogenesis in Myc;sgTp53-driven HCC mouse model as well as xenografted human HCCs, leading to the dampening of HCC burden. Using PST, we further report a marked effect on metastatic HCC outgrowth in the lung along with a reduction of the migratory potential of human HCC cells in 2D and 3D settings. Most notably, our animal models show improvement in local and metastatic survival rates. Similar to other ruthenium-based metallodrugs[64-66], PST was well-tolerated by mice and human cells, suggesting good potential for clinical utilization. We and others have previously demonstrated that PST treatment closely mimics phenotypes fostered by ablation of the plectin gene[18,28,67,68]. Consistently, PST-mediated inhibition of plectin attenuates FAK, MAPK/Erk, and PI3K/Akt pathways in HCC cells with efficacy comparable to CRISPR/Cas-9-engineered functional (ΔIFBD) or full (KO) knockouts. However, despite high PST target selectivity for plectin[67], our data do not rule out pleiotropic effects of PST in the liver and further studies will be required to investigate whether PST mode-of-action in HCC entails molecular mechanisms other than engaging prooncogenic signaling cascades.

Materials and methods

Patient tissue samples

Formalin-fixed paraffin-embedded (FFPE) human liver tissue specimens were prepared at the Department of Surgery of the University Hospital Mannheim. The cohort consisted of 21 patients diagnosed with HCC (for details, see Supplementary file 1). Tissue collection and analysis were performed in accordance with institutional review board guidelines (reference no. 2012-293N-MA), and written informed consent was obtained from all included patients.

Animals

Liver-specific deletion of the plectin (Plec) gene was achieved by crossing *Plectin*$^{flox/flox}$ mice (*Ple*$^{fl/fl}$)[69] with *Alb-Cre* transgenic mice (MGI 2176228; The Jackson Laboratory, Bar Harbor, ME) to generate *Plectin*$^{lox/lox/Alb\text{-}Cre}$ (*Ple*$^{\Delta Alb}$) mice[26]. Immunodeficient NOD.Cg-Prkdcscid Il2rgtm1Wjl/SzJ (NSG) mice were purchased from the Czech Centre for Phenogenomics (BIOCEV – Institute of Molecular Genetics Academy of Sciences, Prague, Czechia)

Animals were housed under specific pathogen-free conditions with regular access to chow and drinking water and 12 h light/12 h dark conditions. All animal studies were performed in accordance with European Directive 86/609/EEC and were approved by the Czech Central Commission for Animal Welfare. Age-matched littermate mice were used in all experiments. The details regarding animal treatments can be found in the following sections.

DEN-induced HCC mouse model

2-week-old *Ple*$^{fl/fl}$ and *Ple*$^{\Delta Alb}$ mice received intraperitoneal injection of 25 mg/kg diethylnitrosamine (DEN; Sigma-Aldrich, St. Louis, MO, USA) diluted in PBS. Mice were monitored for tumor formation 30 and 42 weeks after the DEN injection by magnetic resonance imaging (MRI) and tumor volumes were calculated from MRI images (for details see Magnetic resonance imaging section). Mice were sacrificed at 44 weeks post-injection, livers were dissected, and tumors were measured using a caliper.

Lung colonization assay

Huh7 and SNU-475 cell lines stably expressing Red Firefly Luciferase reporter and GFP were prepared by lentiviral transfection of LentiGlo™ pLenti-CMV-RedFluc-IRES-EGFP plasmid (LP-31, Targeting Systems, El Cajon, CA, USA) according to the manufacturer´s protocol. Next, 2×10^6 Huh7 or SNU-475 cells suspended in serum-free Dulbecco's modified Eagle medium (DMEM, Sigma-Aldrich) were injected into the tail vein of 5-week-old NSG mice. The mice were monitored for survival analysis or monitored using bioluminescence imaging for the presence of lung metastasis after 5 weeks. Prior to

imaging, mice were anesthetized with isoflurane and injected intraperitoneally with D-luciferin potassium salt (Promega, Madison, WI, USA). Ten to fifteen min after injection, luciferase activity was measured using LagoX (Spectral Instruments Imaging, Tuscon, AZ, USA).

HDTVi-induced HCC mouse model

For hydrodynamic tail vein injections, a mixture of plasmid mix containing 5 µg/ml of px330 expressing Tp53 sgRNA, 5 µg/ml of pT3-EF1a MYC DNA (92046, Addgene, Watertown, MA, USA), and 0.5 µg/ml pCMV HSB2 sleeping beauty transponase was prepared in a sterile 0.9% sodium chloride (NaCl) solution. 7-week-old $Ple^{fl/fl}$ and $Ple^{\Delta Alb}$ mice were pre-warmed for 15 min using two infrared lamps (IL 11, Beuer GmbH, Ulm, Germany), placed in a restrainer (TV-RED-150_STD, Braintree Scientific INC., Braintree, MA, USA) and injected intravenously via the lateral tail vein with a total volume corresponding to 10% of body weight over 5–7 s. All animals were monitored daily, and animal experiments were performed in compliance with all relevant ethical regulations outlined in the animal permit. After mice were sacrificed, livers and lungs were visually inspected, excised, and photographed. Tumor samples were taken to obtain protein, and the remaining liver tissue was incubated in 4% PFA for at least 24 h for FFPE tissue preparation.

Statistical analyses

All data mining with the exception of patient analysis, proteomics on mouse tissue samples, and proteomics of SNU-475 cell cultures (see details in corresponding sections), all graphs and statistical tests were performed using GraphPad Prism (GraphPad Software, Inc., La Jolla, CA). In the boxplots, the box margins represent the 25th and 75th percentile with the midline indicates the median. Whiskers reach the last data point. Data comparison of adjacent tumor and non-tumor tissue was performed using a paired *t*-test. Data comparison of individual experimental groups with the control group was performed using a two-tailed *t*-test. Growth curves were analyzed using Two-way ANOVA. Survival curves were analyzed using the Mantel-Cox test. Data distributions were assumed to be normal, but this was not formally tested. Statistical significance was determined at the level of $*P < 0.05$, $**P < 0.01$, $\dagger P < 0.001$. The number of independent experiments (N), number of data points (n), and statistical tests used are specified for individual experiments in the figure legends.

For further details regarding the materials used, please refer to the supplementary information.

Acknowledgement

We would like to thank D. Tschaharganeh (DKFZ, Heidelberg) for generously providing the px330 (Tp53 sgRNA) and pT3-EF1a MYC plasmids, and B. Schuster (IMG CAS, Prague) for pX330 Cas9-Venus plasmid; D. Heide and J. Hetzer (DKFZ, Heidelberg) for their outstanding technical assistance; B. Fabry (FAU Erlangen-Nürnberg), K. Volz (DKFZ, Heidelberg), J. Prochazka (Czech Centre for Phenogenomics, Vestec), M. Maninova, M. K. Adamcova, M. Burocziova, M. Capek, and J. Valecka (all IMG CAS, Prague) for their expertise. We acknowledge the Light Microscopy Core Facility, IMG CAS, Prague, Czech Republic, for support with advanced microscopy imaging.

Competing interests The authors have declared that no conflict of interest exists.

Funding This work was supported by the Grant Agency of the Czech Republic (GA21-21736S and GA24-10672S); the Institutional Research Project of the Czech Academy of Sciences (RVO 68378050); National Institute for Cancer Research (Programme EXCELES, LX22NPO5102) - Funded by the European Union - Next Generation EU; MEYS CR projects (LM2023050, LM2018126, LQ1604 NPU II, LO1419, and LM2015040); and MEYS CR/ERDF projects (OP RDI CZ.1.05/2.1.00/19.0395 and CZ.1.05/1.1.00/02.0109).

Author contributions Study concept and design: M.G. Acquisition of data: Z.O., G.O.-E., K.K., M.P., L.S., P.B., P.N., P.B., Y.B., A.B., C.G., B.K., A.G., K.S., M.O., O.T., N.J. Analysis and interpretation of data: Z.O., K.K., M.P., L.F., J.K., E.S., D.J., O.T., N.J., D.R., S.M.M., M.G. Drafting of the manuscript: Z.O., M.G. Critical revision of the manuscript for important intellectual content: all authors. Funding: M.G., S.M.M., D.R. Technical and material support: J.K., M.J., M.R., N.R., E.B., A.B., T.O., D.J., M.H., G.W., S.M.M.

References

1 Broders-Bondon, F., Nguyen Ho-Bouldoires, T. H., Fernandez-Sanchez, M. E. & Farge, E. Mechanotransduction in tumor progression: The dark side of the force. *J Cell Biol* **217**, 1571-1587, doi:10.1083/jcb.201701039 (2018).

2 Piersma, B., Hayward, M. K. & Weaver, V. M. Fibrosis and cancer: A strained relationship. *Biochim Biophys Acta Rev Cancer* **1873**, 188356, doi:10.1016/j.bbcan.2020.188356 (2020).

3 Cooper, J. & Giancotti, F. G. Integrin Signaling in Cancer: Mechanotransduction, Stemness, Epithelial Plasticity, and Therapeutic Resistance. *Cancer Cell* **35**, 347-367, doi:10.1016/j.ccell.2019.01.007 (2019).

4 Hoxhaj, G. & Manning, B. D. The PI3K-AKT network at the interface of oncogenic signalling and cancer metabolism. *Nat Rev Cancer* **20**, 74-88, doi:10.1038/s41568-019-0216-7 (2020).

5 Sun, Z., Guo, S. S. & Fassler, R. Integrin-mediated mechanotransduction. *J Cell Biol* **215**, 445-456, doi:10.1083/jcb.201609037 (2016).

6 Dupont, S. *et al.* Role of YAP/TAZ in mechanotransduction. *Nature* **474**, 179-183, doi:10.1038/nature10137 (2011).

7 Esnault, C. *et al.* Rho-actin signaling to the MRTF coactivators dominates the immediate transcriptional response to serum in fibroblasts. *Genes Dev* **28**, 943-958, doi:10.1101/gad.239327.114 (2014).

8 Bustelo, X. R. RHO GTPases in cancer: known facts, open questions, and therapeutic challenges. *Biochem Soc Trans* **46**, 741-760, doi:10.1042/BST20170531 (2018).

9 Bouameur, J. E., Favre, B. & Borradori, L. Plakins, a versatile family of cytolinkers: roles in skin integrity and in human diseases. *J Invest Dermatol* **134**, 885-894, doi:10.1038/jid.2013.498 (2014).

10 Prechova, M., Korelova, K. & Gregor, M. Plectin. *Curr Biol* **33**, R128-R130, doi:10.1016/j.cub.2022.12.061 (2023).

11 Gundesli, H., Kori, M. & Arga, K. Y. The Versatility of Plectin in Cancer: A Pan-Cancer Analysis on Potential Diagnostic and Prognostic Impacts of Plectin Isoforms. *OMICS* **27**, 281-296, doi:10.1089/omi.2023.0053 (2023).

12 Perez, S. M., Brinton, L. T. & Kelly, K. A. Plectin in Cancer: From Biomarker to Therapeutic Target. *Cells* **10**, doi:10.3390/cells10092246 (2021).

13 Andra, K., Nikolic, B., Stocher, M., Drenckhahn, D. & Wiche, G. Not just scaffolding: plectin regulates actin dynamics in cultured cells. *Genes Dev* **12**, 3442-3451, doi:10.1101/gad.12.21.3442 (1998).

14 Nikolic, B., Mac Nulty, E., Mir, B. & Wiche, G. Basic amino acid residue cluster within nuclear targeting sequence motif is essential for cytoplasmic plectin-vimentin network junctions. *J Cell Biol* **134**, 1455-1467, doi:10.1083/jcb.134.6.1455 (1996).

15 Eisenberg, J. L. *et al.* Plectin-containing, centrally localized focal adhesions exert traction forces in primary lung epithelial cells. *J Cell Sci* **126**, 3746-3755, doi:10.1242/jcs.128975 (2013).

16 Na, S. *et al.* Plectin contributes to mechanical properties of living cells. *Am J Physiol Cell Physiol* **296**, C868-877, doi:10.1152/ajpcell.00604.2008 (2009).

17 Osmanagic-Myers, S. *et al.* Plectin reinforces vascular integrity by mediating crosstalk between the vimentin and the actin networks. *J Cell Sci* **128**, 4138-4150, doi:10.1242/jcs.172056 (2015).

18 Prechova, M. *et al.* Plectin-mediated cytoskeletal crosstalk controls cell tension and cohesion in epithelial sheets. *The Journal of cell biology* **221**, doi:10.1083/jcb.202105146 (2022).

19 De Pascalis, C. *et al.* Intermediate filaments control collective migration by restricting traction forces and sustaining cell-cell contacts. *J Cell Biol* **217**, 3031-3044, doi:10.1083/jcb.201801162 (2018).

20 Gregor, M. *et al.* Mechanosensing through focal adhesion-anchored intermediate filaments. *FASEB J* **28**, 715-729, doi:10.1096/fj.13-231829 (2014).

21 Wang, W. *et al.* Hemidesmosomes modulate force generation via focal adhesions. *J Cell Biol* **219**, doi:10.1083/jcb.201904137 (2020).
22 Marks, P. C., Hewitt, B. R., Baird, M. A., Wiche, G. & Petrie, R. J. Plectin linkages are mechanosensitive and required for the nuclear piston mechanism of three-dimensional cell migration. *Mol Biol Cell* **33**, ar104, doi:10.1091/mbc.E21-08-0414 (2022).
23 Vahidnezhad, H. *et al.* Mutation update: The spectra of PLEC sequence variants and related plectinopathies. *Human mutation* **43**, 1706-1731, doi:10.1002/humu.24434 (2022).
24 Boyault, S. *et al.* Transcriptome classification of HCC is related to gene alterations and to new therapeutic targets. *Hepatology* **45**, 42-52, doi:10.1002/hep.21467 (2007).
25 Chiang, D. Y. *et al.* Focal gains of VEGFA and molecular classification of hepatocellular carcinoma. *Cancer Res* **68**, 6779-6788, doi:10.1158/0008-5472.CAN-08-0742 (2008).
26 Jirouskova, M. *et al.* Plectin controls biliary tree architecture and stability in cholestasis. *Journal of hepatology* **68**, 1006-1017, doi:10.1016/j.jhep.2017.12.011 (2018).
27 Xu, R. *et al.* Plectin Downregulation Inhibits Migration and Suppresses Epithelial Mesenchymal Transformation of Hepatocellular Carcinoma Cells via ERK1/2 Signaling. *Int J Mol Sci* **24**, doi:10.3390/ijms24010073 (2022).
28 Meier, S. M. *et al.* An Organoruthenium Anticancer Agent Shows Unexpected Target Selectivity For Plectin. *Angewandte Chemie (International ed. in English)* **56**, 8267-8271, doi:10.1002/anie.201702242 (2017).
29 Jiu, Y. *et al.* Bidirectional Interplay between Vimentin Intermediate Filaments and Contractile Actin Stress Fibers. *Cell Rep* **11**, 1511-1518, doi:10.1016/j.celrep.2015.05.008 (2015).
30 Burgstaller, G., Gregor, M., Winter, L. & Wiche, G. Keeping the vimentin network under control: cell-matrix adhesion-associated plectin 1f affects cell shape and polarity of fibroblasts. *Mol Biol Cell* **21**, 3362-3375, doi:10.1091/mbc.E10-02-0094 (2010).
31 Bodor, D. L., Ponisch, W., Endres, R. G. & Paluch, E. K. Of Cell Shapes and Motion: The Physical Basis of Animal Cell Migration. *Dev Cell* **52**, 550-562, doi:10.1016/j.devcel.2020.02.013 (2020).
32 Yolland, L. *et al.* Persistent and polarized global actin flow is essential for directionality during cell migration. *Nat Cell Biol* **21**, 1370-1381, doi:10.1038/s41556-019-0411-5 (2019).
33 Revia, S. *et al.* Histone H3K27 demethylase KDM6A is an epigenetic gatekeeper of mTORC1 signalling in cancer. *Gut* **71**, 1613-1628, doi:10.1136/gutjnl-2021-325405 (2022).
34 Subramanian, A. *et al.* Gene set enrichment analysis: a knowledge-based approach for interpreting genome-wide expression profiles. *Proc Natl Acad Sci U S A* **102**, 15545-15550, doi:10.1073/pnas.0506580102 (2005).
35 Llovet, J. M. *et al.* Hepatocellular carcinoma. *Nat Rev Dis Primers* **7**, 6, doi:10.1038/s41572-020-00240-3 (2021).
36 Singal, A. G. *et al.* AASLD Practice Guidance on prevention, diagnosis, and treatment of hepatocellular carcinoma. *Hepatology* **78**, 1922-1965, doi:10.1097/HEP.0000000000000466 (2023).
37 Ladd, A. D., Duarte, S., Sahin, I. & Zarrinpar, A. Mechanisms of drug resistance in HCC. *Hepatology* **79**, 926-940, doi:10.1097/HEP.0000000000000237 (2024).
38 Liu, Y. H. *et al.* Cytokeratin 18-mediated disorganization of intermediate filaments is induced by degradation of plectin in human liver cells. *Biochem Biophys Res Commun* **407**, 575-580, doi:10.1016/j.bbrc.2011.03.066 (2011).
39 Uhlen, M. *et al.* A pathology atlas of the human cancer transcriptome. *Science* **357**, doi:10.1126/science.aan2507 (2017).
40 Flores, I. L. *et al.* EEF1D modulates proliferation and epithelial-mesenchymal transition in oral squamous cell carcinoma. *Clin Sci (Lond)* **130**, 785-799, doi:10.1042/CS20150646 (2016).
41 Yang, Z. *et al.* Putative biomarkers of malignant transformation of sinonasal inverted papilloma into squamous cell carcinoma. *J Int Med Res* **47**, 2371-2380, doi:10.1177/0300060519838385 (2019).

42 Paumard-Hernandez, B. *et al.* Whole exome sequencing identifies PLEC, EXO5 and DNAH7 as novel susceptibility genes in testicular cancer. *Int J Cancer* **143**, 1954-1962, doi:10.1002/ijc.31604 (2018).

43 Yin, X., Kong, L. & Liu, P. Identification of prognosis-related molecular subgroups based on DNA methylation in pancreatic cancer. *Clin Epigenetics* **13**, 109, doi:10.1186/s13148-021-01090-w (2021).

44 Strouhalova, K. *et al.* Vimentin Intermediate Filaments as Potential Target for Cancer Treatment. *Cancers (Basel)* **12**, doi:10.3390/cancers12010184 (2020).

45 Tolba, R., Kraus, T., Liedtke, C., Schwarz, M. & Weiskirchen, R. Diethylnitrosamine (DEN)-induced carcinogenic liver injury in mice. *Lab Anim* **49**, 59-69, doi:10.1177/0023677215570086 (2015).

46 Lee, J. S. *et al.* Application of comparative functional genomics to identify best-fit mouse models to study human cancer. *Nat Genet* **36**, 1306-1311, doi:10.1038/ng1481 (2004).

47 Moon, S. H. *et al.* p53 Represses the Mevalonate Pathway to Mediate Tumor Suppression. *Cell* **176**, 564-580 e519, doi:10.1016/j.cell.2018.11.011 (2019).

48 Buckup, M. *et al.* Plectin is a regulator of prostate cancer growth and metastasis. *Oncogene* **40**, 663-676, doi:10.1038/s41388-020-01557-9 (2021).

49 Pal, K. *et al.* Multifaceted peptide assisted one-pot synthesis of gold nanoparticles for plectin-1 targeted gemcitabine delivery in pancreatic cancer. *Nanoscale* **9**, 15622-15634, doi:10.1039/c7nr03172f (2017).

50 Perez, S. M., Dimastromatteo, J., Landen, C. N., Jr. & Kelly, K. A. A Novel Monoclonal Antibody Targeting Cancer-Specific Plectin Has Potent Antitumor Activity in Ovarian Cancer. *Cells* **10**, doi:10.3390/cells10092218 (2021).

51 Abrahamsberg, C. *et al.* Targeted ablation of plectin isoform 1 uncovers role of cytolinker proteins in leukocyte recruitment. *Proc Natl Acad Sci U S A* **102**, 18449-18454, doi:10.1073/pnas.0505380102 (2005).

52 Zrelski, M. M. *et al.* Plectin Deficiency in Fibroblasts Deranges Intermediate Filament and Organelle Morphology, Migration, and Adhesion. *J Invest Dermatol* **144**, 547-562 e549, doi:10.1016/j.jid.2023.08.020 (2024).

53 Katada, K. *et al.* Plectin promotes migration and invasion of cancer cells and is a novel prognostic marker for head and neck squamous cell carcinoma. *J Proteomics* **75**, 1803-1815, doi:10.1016/j.jprot.2011.12.018 (2012).

54 McInroy, L. & Maatta, A. Plectin regulates invasiveness of SW480 colon carcinoma cells and is targeted to podosome-like adhesions in an isoform-specific manner. *Exp Cell Res* **317**, 2468-2478, doi:10.1016/j.yexcr.2011.07.013 (2011).

55 Sutoh Yoneyama, M. *et al.* Vimentin intermediate filament and plectin provide a scaffold for invadopodia, facilitating cancer cell invasion and extravasation for metastasis. *Eur J Cell Biol* **93**, 157-169, doi:10.1016/j.ejcb.2014.03.002 (2014).

56 Wenta, T. *et al.* Disassembly of alpha6beta4-mediated hemidesmosomal adhesions promotes tumorigenesis in PTEN-negative prostate cancer by targeting plectin to focal adhesions. *Oncogene* **41**, 3804-3820, doi:10.1038/s41388-022-02389-5 (2022).

57 Bhattacharya, R. *et al.* Recruitment of vimentin to the cell surface by beta3 integrin and plectin mediates adhesion strength. *J Cell Sci* **122**, 1390-1400, doi:10.1242/jcs.043042 (2009).

58 Burch, T. C., Watson, M. T. & Nyalwidhe, J. O. Variable metastatic potentials correlate with differential plectin and vimentin expression in syngeneic androgen independent prostate cancer cells. *PLoS One* **8**, e65005, doi:10.1371/journal.pone.0065005 (2013).

59 Cappuyns, S., Corbett, V., Yarchoan, M., Finn, R. S. & Llovet, J. M. Critical Appraisal of Guideline Recommendations on Systemic Therapies for Advanced Hepatocellular Carcinoma: A Review. *JAMA oncology* **10**, 395-404, doi:10.1001/jamaoncol.2023.2677 (2024).

60 Llovet, J. M., Montal, R., Sia, D. & Finn, R. S. Molecular therapies and precision medicine for hepatocellular carcinoma. *Nat Rev Clin Oncol* **15**, 599-616, doi:10.1038/s41571-018-0073-4 (2018).

61 Llovet, J. M. *et al.* Sorafenib in advanced hepatocellular carcinoma. *N Engl J Med* **359**, 378-390, doi:10.1056/NEJMoa0708857 (2008).

62 Yau, T., Chan, P., Epstein, R. & Poon, R. T. Evolution of systemic therapy of advanced hepatocellular carcinoma. *World J Gastroenterol* **14**, 6437-6441, doi:10.3748/wjg.14.6437 (2008).

63 Yau, T. *et al.* Nivolumab in advanced hepatocellular carcinoma: Sorafenib-experienced Asian cohort analysis. *J Hepatol* **71**, 543-552, doi:10.1016/j.jhep.2019.05.014 (2019).

64 Bakewell, S. J. *et al.* Suppression of stress induction of the 78-kilodalton glucose regulated protein (GRP78) in cancer by IT-139, an anti-tumor ruthenium small molecule inhibitor. *Oncotarget* **9**, 29698-29714, doi:10.18632/oncotarget.25679 (2018).

65 Burris, H. A. *et al.* Safety and activity of IT-139, a ruthenium-based compound, in patients with advanced solid tumours: a first-in-human, open-label, dose-escalation phase I study with expansion cohort. *ESMO Open* **1**, e000154, doi:10.1136/esmoopen-2016-000154 (2016).

66 Flocke, L. S., Trondl, R., Jakupec, M. A. & Keppler, B. K. Molecular mode of action of NKP-1339 - a clinically investigated ruthenium-based drug - involves ER- and ROS-related effects in colon carcinoma cell lines. *Invest New Drugs* **34**, 261-268, doi:10.1007/s10637-016-0337-8 (2016).

67 Meier-Menches, S. M. *et al.* Time-dependent shotgun proteomics revealed distinct effects of an organoruthenium prodrug and its activation product on colon carcinoma cells. *Metallomics* **11**, 118-127, doi:10.1039/c8mt00152a (2019).

68 Wernitznig, D. *et al.* Plecstatin-1 induces an immunogenic cell death signature in colorectal tumour spheroids. *Metallomics* **12**, 2121-2133, doi:10.1039/d0mt00227e (2020).

69 Ackerl, R. *et al.* Conditional targeting of plectin in prenatal and adult mouse stratified epithelia causes keratinocyte fragility and lesional epidermal barrier defects. *Journal of cell science* **120**, 2435-2443, doi:10.1242/jcs.004481 (2007).

Figures & Figure legends

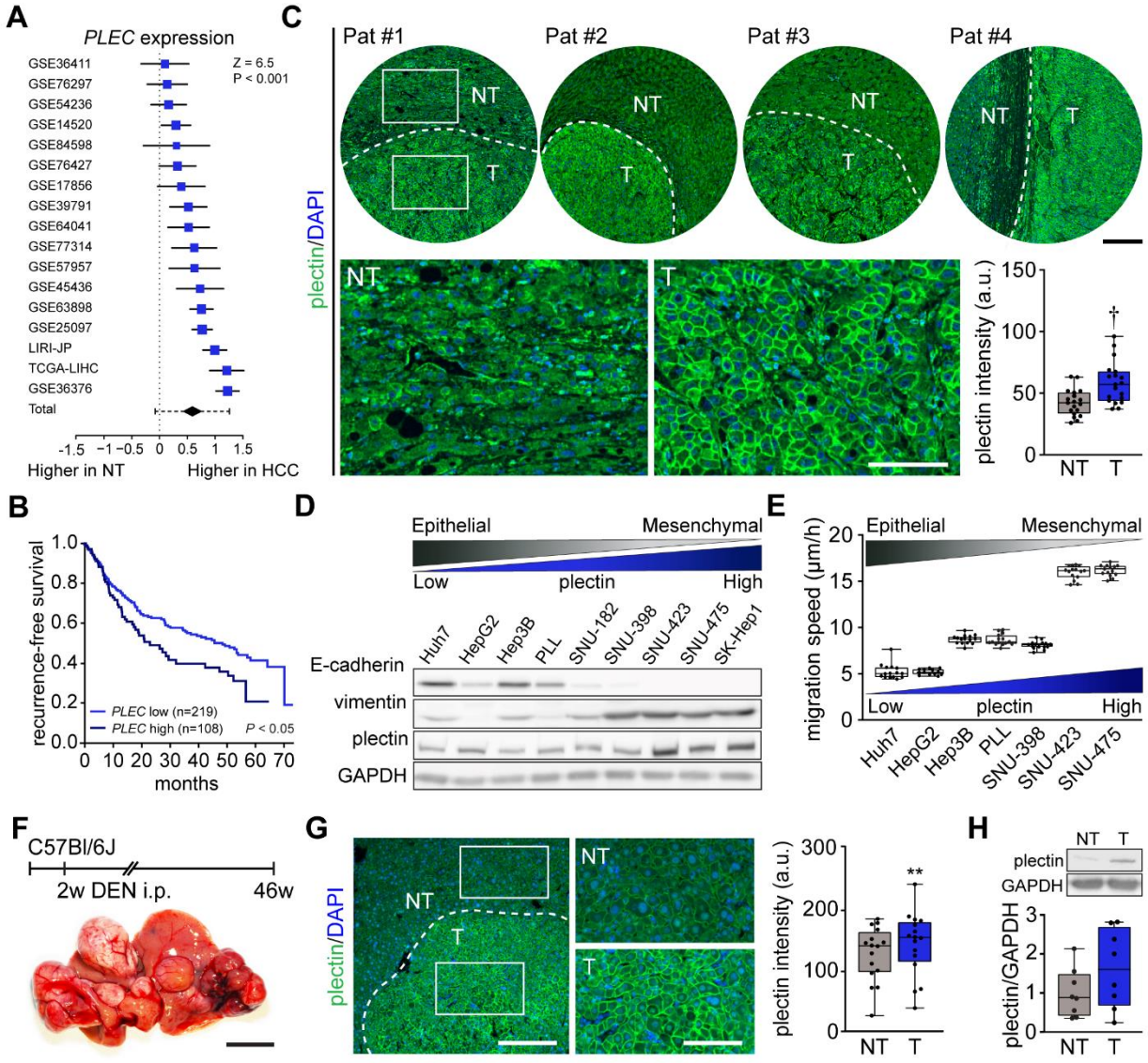

Figure 1. Plectin elevation in tumor hepatocytes is associated with HCC progression and poor prognosis. (A) Meta-analysis of differential *plectin* (*PLEC*) mRNA expression in non-tumor (NT) liver and hepatocellular carcinoma (HCC) patients. Blue squares indicate the standardized mean difference (SMD) and 95% confidence interval of individual datasets. The black diamond shows the mean and 95% confidence interval for the combined SMD, while the whiskers indicate the 95% prediction interval. **(B)** Kaplan-Meier curve of recurrence-free survival of HCC patients with low *PLEC* (lower 2 tertiles, *n* = 219) and high *PLEC* (top tertile, *n* = 108) mRNA expression. Log-rank test; $P < 0.05$. **(C)** Representative images of human HCC tissue sections immunolabeled for plectin (green). Nuclei, DAPI (blue). Dashed line, the borderline between non-tumor (NT) and tumor (T) area. Boxed areas, x4 images. Scale bars, 200 and 100 µm (boxed areas). Boxplot shows quantification of plectin fluorescence intensities in NT and T areas. The box represents the median, 25th, and 75th percentile;

whiskers reach the last data point; dots, individual patients; *N* = 19. Paired two-tailed *t*-test; †*P* < 0.001. **(D)** Immunoblot analysis of indicated HCC cell lines with antibodies to plectin, E-cadherin, and vimentin. GAPDH, loading control. **(E)** Quantification of the speed of indicated HCC cell lines migrating in the scratch-wound assay. Boxplots show the median, 25th, and 75th percentile with whiskers reaching the last data point; dots, fields of view; *n* = 15 (Huh7), 13 (HepG2), 15 (Hep3B), 15 (PLL), 15 (SNU-398), 15 (SNU-423), 15 (SNU-475) fields of view; *N* = 3. **(F)** Hepatocarcinogenesis was induced in two-week-old C57Bl/6J mice by intraperitoneal injection of DEN. Representative image of the livers with multifocal HCC at 46 weeks post-induction. Scale bar, 1 cm. **(G)** Representative image of DEN-induced HCC section immunolabeled for plectin (green). Nuclei, DAPI (blue). Dashed line, the borderline between non-tumor (NT) and tumor (T) area. Boxed areas, x2 images. Scale bars, 200 and 100 µm (boxed areas). Quantification of plectin fluorescence intensities in NT and T areas. Boxplot shows the median, 25th, and 75th percentile with whiskers reaching the last data point; dots, fields of view; *n* = 16 fields of view; *N* = 4. Paired two-tailed *t*-test; **$P < 0.01$. **(H)** Immunoblot analysis of NT and T liver lysates. The boxplot shows relative plectin band intensities normalized to GAPDH. The box represents the median, 25th, and 75th percentile; whiskers reach the last data point; dots, individual mice; *N* = 8.

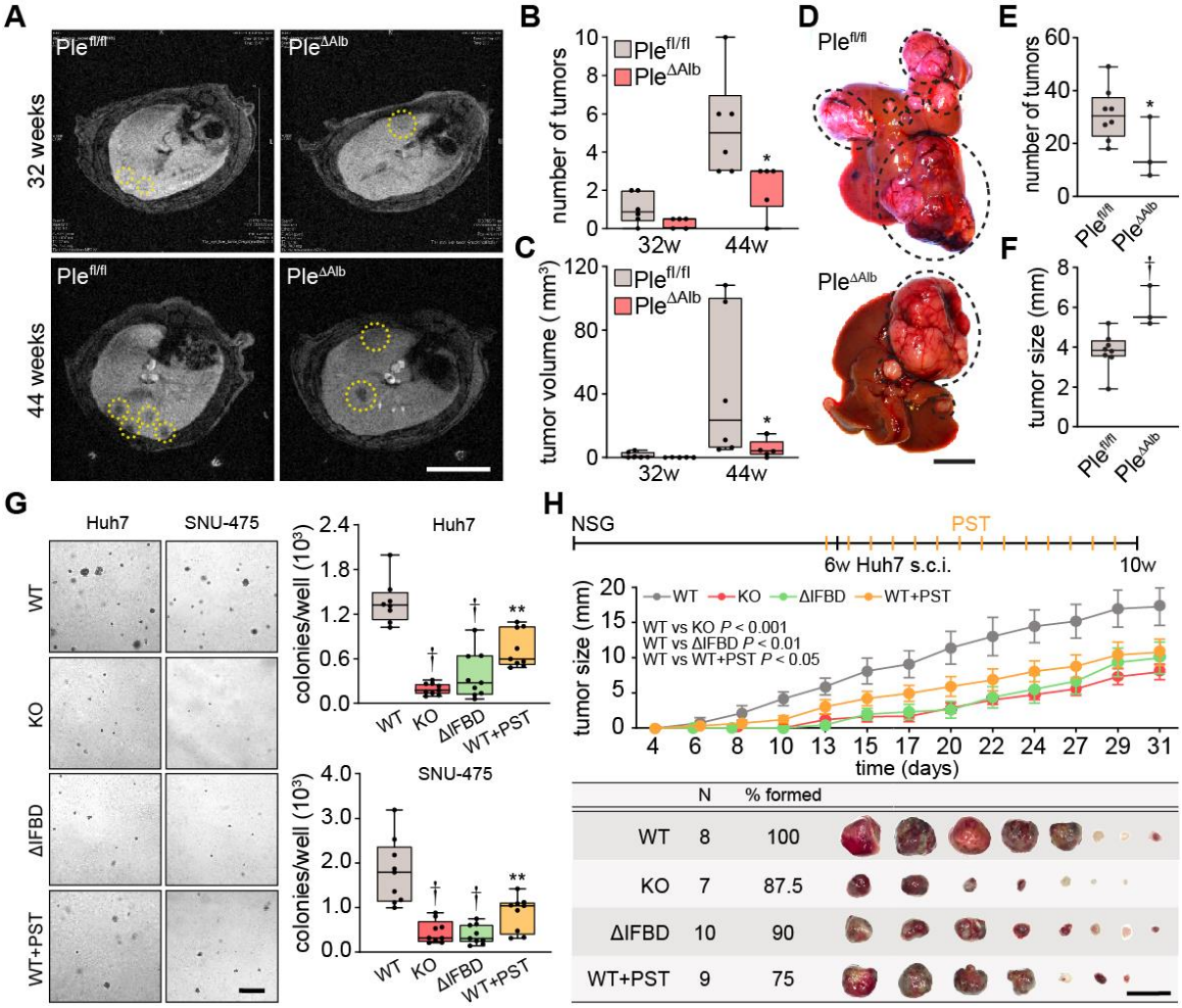

Figure 2. Plectin promotes HCC growth. (A) Representative MRI images of *Ple*$^{fl/fl}$ and *Ple*$^{\Delta Alb}$ livers at 32 and 44 weeks post-DEN injection. Dashed circles, tumors. Scale bar, 500 µm. **(B, C)** Quantification of tumor number (B) and volume (C) in *Ple*$^{fl/fl}$ and *Ple*$^{\Delta Alb}$ livers shown in (A). Boxplot shows the median, 25th, and 75th percentile with whiskers reaching the last data point; dots, individual mice; N = 6 (*Ple*$^{fl/fl}$), 5 (*Ple*$^{\Delta Alb}$). Two-tailed t-test; *P < 0.05. **(D)** Representative images of *Ple*$^{fl/fl}$ and *Ple*$^{\Delta Alb}$ livers at 44 weeks post-induction. Dashed circles, tumors. Scale bar, 1 cm. **(E, F)** Quantification of the number (E) and size (F) of *Ple*$^{fl/fl}$ and *Ple*$^{\Delta Alb}$ tumors shown in (D). Boxplot shows the median, 25th, and 75th percentile with whiskers reaching the last data point; dots, individual mice; N = 8 (*Ple*$^{fl/fl}$), 3 (*Ple*$^{\Delta Alb}$). Two-tailed t-test; *P < 0.05; †P < 0.001. **(G)** Representative images of colonies from WT, KO, ΔIFBD, and PST-treated WT (WT+PST) Huh7 and SNU-475 cells grown in soft agar. Scale bar, 500 µm. Boxplots show the number of Huh7 (upper graph) and SNU-475 (lower graph) cell colonies. The box represents the median, 25th, and 75th percentile with whiskers reaching the last data point; dots, agar wells; n = 9 agar wells; N = 3. Two-tailed t-test; **P < 0.01; †P < 0.001. **(H)** Six-week-old NSG mice were subcutaneously injected with indicated Huh7 cells into both hind flanks and were kept either untreated (WT, KO, and ΔIFBD) or daily treated by orogastric gavage of plecstatin (WT+PST) as

indicated in upper bar. Mice were sacrificed 4 weeks post-injection and xenografts were dissected. The graph shows the time course of xenograft growth. Data are shown as mean ± SEM; n = 8 (WT), 7 (KO), 10 (ΔIFBD) and 9 (WT+PST) tumors; *N* = 4 (WT), 4 (KO), 5 (ΔIFBD) and 6 (WT+PST). Two-way ANOVA. The table shows the number (N), percentage, and representative images of formed xenografts. Scale bar, 2 cm.

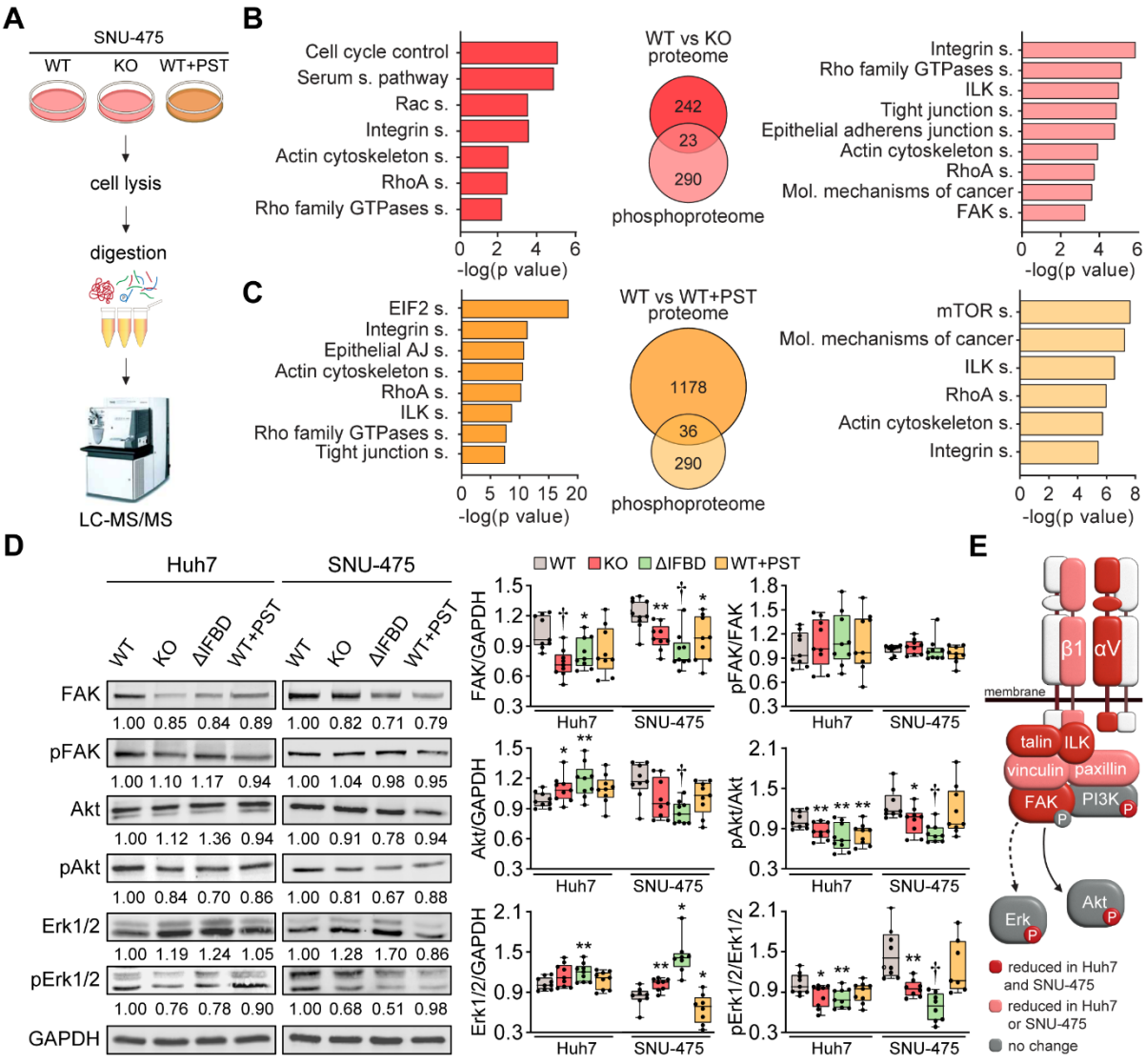

Figure 3. CRISPR/Cas9- or PST-mediated plectin inactivation attenuates HCC oncogenic potential through FAK, Erk1/2, and PI3K/Akt axis. (A) Schematic of MS-based proteomic analysis of WT, KO, and PST-treated WT (WT+PST) SNU-475 cells. **(B,C)** Ingenuity Pathway Analysis (IPA) canonical signaling pathways predicted from differentially expressed proteins identified by proteomics (left) and phosphoproteomics (right) in WT vs. KO (B) and WT vs. WT+PST (C) proteomes. Venn diagrams show relative proportions of differentially expressed proteins. Two-sided Student´s *t*-test with multiple testing correction: FDR < 0.05; s0 = 0.1; triplicates. **(D)** Quantification of FAK, phospho-Tyr397-FAK (pFAK), Akt, phospho-Ser473-Akt (pAkt), Erk1/2, and phospho-Thr202/Tyr204-Erk (pErk) in indicated Huh7 and SNU-475 cell lines by immunoblotting. GAPDH, loading control. The numbers below lines indicate relative band intensities normalized to average WT values. Boxplots show relative band intensities normalized to GAPDH or non-phosphorylated protein. The box represents the median, 25th, and 75th percentile with whiskers reaching the last data point; dots, individual experiments; *N*

= 9. Two-tailed *t*-test; **P* < 0.05; ***P* < 0.01; †*P* < 0.001. **(E)** Schematic representation of immunoblot analyses of adhesome-associated signaling shown in (F) and (Extended Data Fig. 2h). Proteins with significantly reduced expression levels and/or phosphorylation status (P) upon plectin inactivation in both HCC cell lines are highlighted in red, proteins with significantly reduced expression levels upon plectin inactivation in either Huh7 or SNU-475 cells are highlighted in pink.

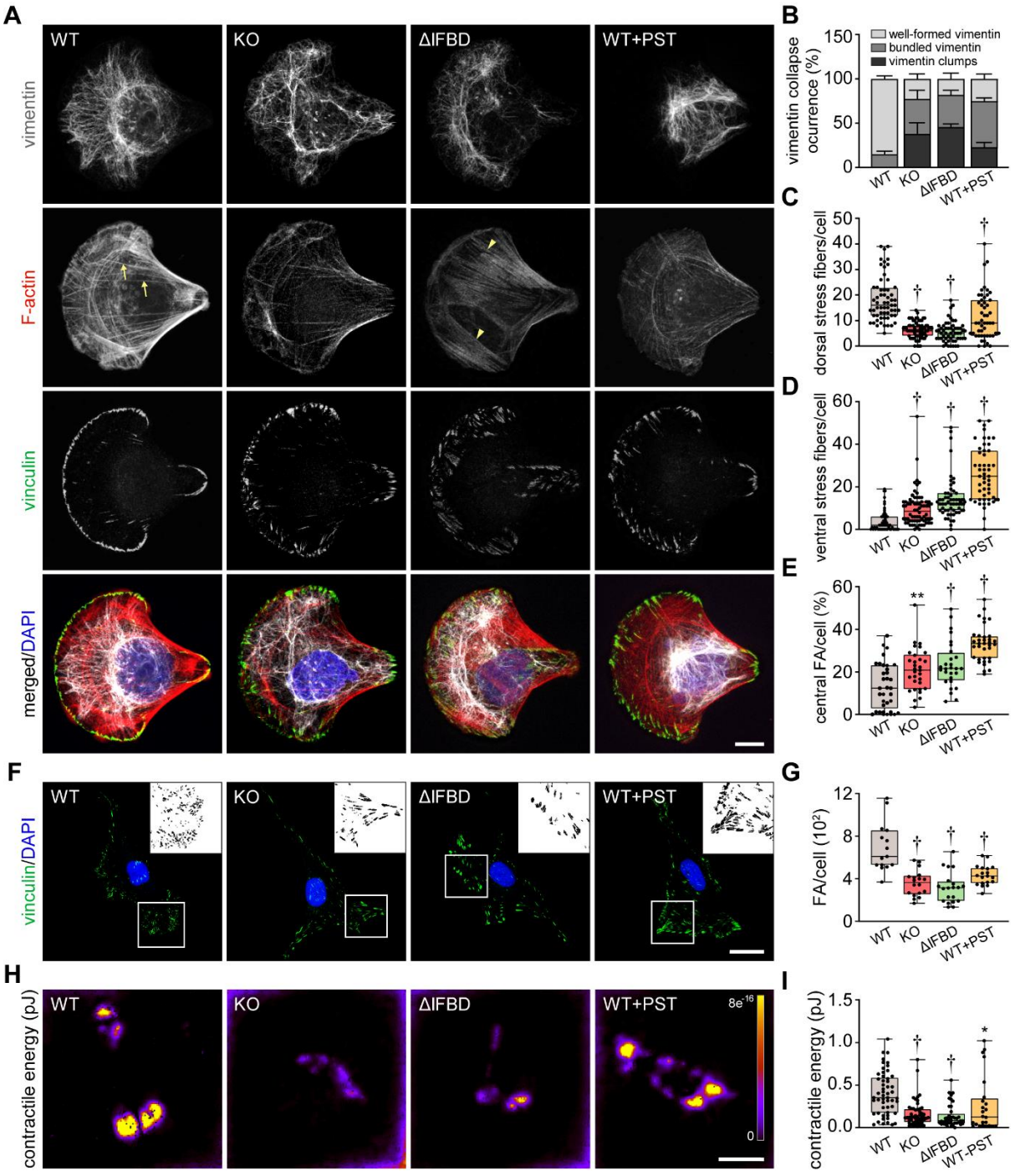

Figure 4. Disruption of cytoskeletal networks upon plectin inactivation accounts for reduced contractility and aberrant adhesions in HCC cells. (A) Representative confocal images of crossbow-shaped fibronectin micropattern-seeded WT, KO, ΔIFBD, and PST-treated WT (WT+PST) SNU-475 cells stained for F-actin (red), vinculin (green), and vimentin (grey). Nuclei, DAPI (blue). Arrows, dorsal stress fibers; arrowheads, ventral stress fibers. Scale bar, 10 µm. **(B)** Quantification of the percentage of cells (shown in (A)) with well-formed, bundled, and clump-containing vimentin networks. Data are shown as mean ± SEM; *n* = 60 (WT), 68 (KO), 55 (ΔIFBD), 50 (WT+PST) cells; *N* = 4 (WT, KO, IFBD), 3 (WT+PST).

(C,D) Quantification of the number of dorsal (C) and ventral (D) actin stress fibers in cells shown in (A). Boxplots show the median, 25th, and 75th percentile with whiskers reaching the last data point; dots, individual cells; *n* = 60 (WT), 68 (KO), 55 (ΔIFBD), 50 (WT+PST); *N* = 4 (WT, KO, IFBD), 3 (WT+PST). Two-tailed *t*-test; †*P* < 0.001. **(E)** Quantification of FAs located within the interior of cells (central) shown in (A). Boxplot shows the median, 25th and 75th percentile with whiskers reaching the last data point; dots, individual cells; *n* = 25 (WT), 26 (KO), 23 (ΔIFBD), 28 (WT+PST); *N* = 3. ****P* < 0.01; †*P* < 0.001. **(F)** Representative confocal images of WT, KO, ΔIFBD, and PST-treated WT (WT+PST) SNU-475 cells immunolabeled for vinculin (green). Nuclei, DAPI (blue). Boxed areas, representative FA clusters shown as segmented binary maps in x2 enlarged insets. Scale bar, 30 µm. **(G)** Quantification of FA number in cells shown in (F). Boxplot shows the median, 25th, and 75th percentile with whiskers reaching the last data point; dots, individual cells; *n* = 15 (WT), 18 (KO), 20 (ΔIFBD), 19 (WT+PST); *N* = 3. Two-tailed *t*-test; †*P* < 0.001. **(H)** Pseudocolor spatial maps of contractile energy determined by TFM in WT, KO, ΔIFBD, and PST-treated WT (WT+PST) SNU-475 cells. Scale bar, 50 µm. **(I)** Quantification of contractile energy in cells shown in (H). Boxplots show the median, 25th, and 75th percentile with whiskers reaching the last data point; dots, individual cells; *n* = 54 (WT), 53 (KO), 41 (ΔIFBD), 24 (WT+PST) cells; *N* = 4. Two-tailed *t* test; **P* < 0.05; ****P* < 0.01; †*P* < 0.001.

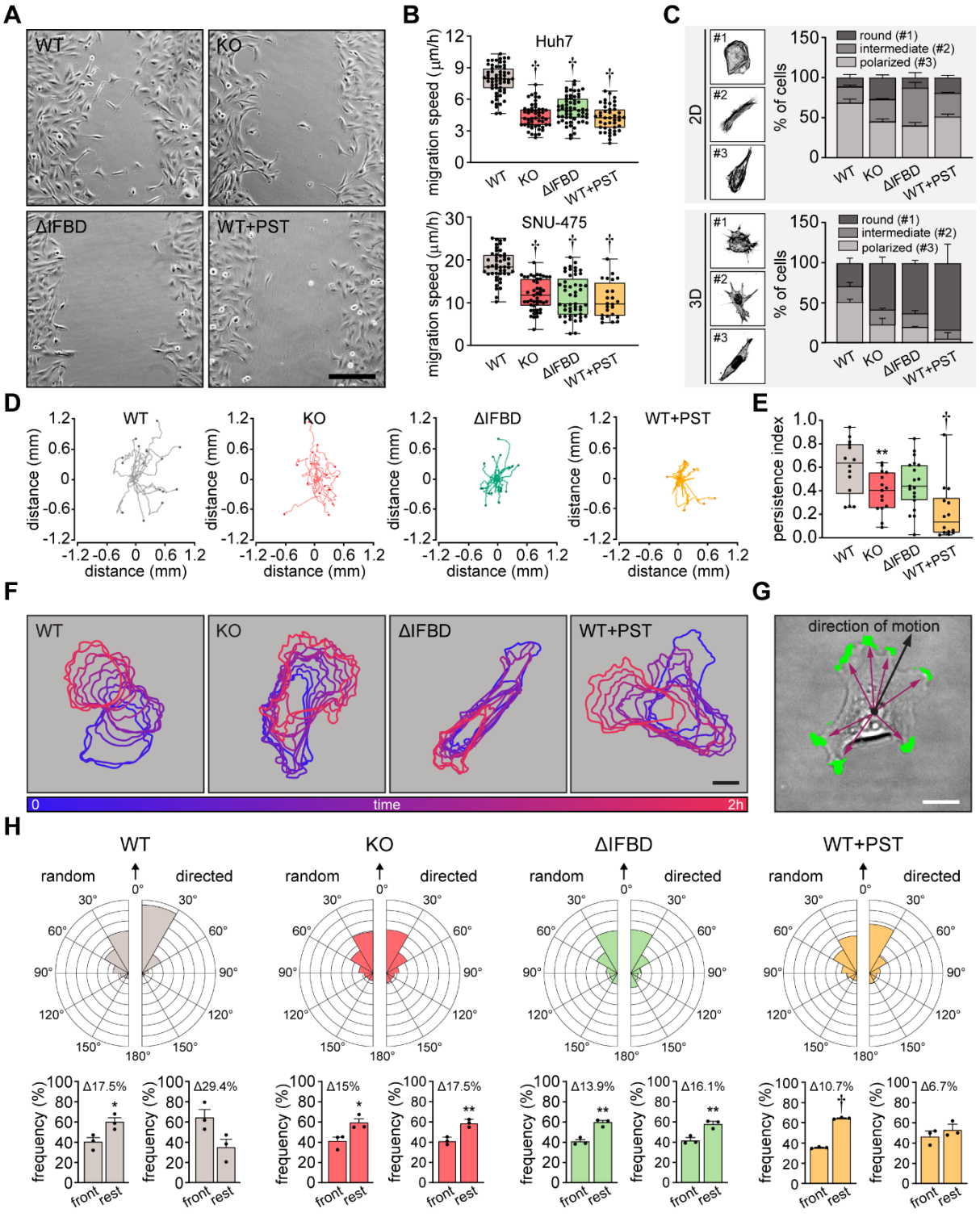

Figure 5. Plectin links migration potential of HCC cells to cell shape dynamics. (A) Representative phase contrast images of WT, KO, ΔIFBD, and PST-treated WT (WT+PST) SNU-475 cells migrating in the scratch-wound assay for 14 hours. Note individual, highly polarized WT cells frequently migrating into scratch areas. Scale bar, 200 µm. **(B)** Quantification of migration speed of indicated Huh7 (upper graph) and SNU-475 (lower graph) cells. Boxplots show the median, 25th, and 75th percentile with

whiskers reaching the last data point; dots, fields of view; *n* (Huh7) = 59 (WT), 51 (KO), 58 (ΔIFBD), 43 (WT+PST); *n* (SNU-475) = 47 (WT), 47 (KO), 50 (ΔIFBD), 24 (WT+PST); *N* (Huh7) = 3; *N* (SNU-475) = 5 (WT, KO, ΔIFBD), 3 (WT+PST). Two-tailed *t*-test; † $P < 0.001$. **(C)** Representative confocal images of F-actin stained WT, KO, ΔIFBD, and PST-treated WT (WT+PST) SNU-475 cells grown on fibronectin-coated coverslips (2D) or in collagen (3D) and classified as round (#1), intermediate (#2), and polarized (#3) shape. Quantification of the percentage of cell shape categories in indicated 2D and 3D SNU-475 cell cultures. Data are shown as mean ± SEM; *N* (2D) = 3; *N* (3D) = 5 (WT), 3 (KO, ΔIFBD), 2 (WT+PST). **(D)** Spider plots with migration trajectories of WT, KO, ΔIFBD, and PST-treated WT (WT+PST) SNU-475 cells tracked during 16 hours of EGF-guided migration; dots, the final position of each single tracked cell. **(E)** Quantification of processivity indices of WT, KO, ΔIFBD, and PST-treated WT (WT+PST) SNU-475 cells. Boxplot shows the median, 25th, and 75th percentile with whiskers reaching the last data point; dots, individual cells; *n* = 15 (WT), 15 (KO), 19 (ΔIFBD), 14 (WT+PST); *N* = 3. Two-tailed *t*-test; **$P < 0.01$;† $P < 0.001$. **(F)** Representative time sequences of the WT, KO, ΔIFBD, and PST-treated WT (WT+PST) SNU-475 cell contours during EGF-guided migration. Color coding indicates the time of cell position acquired in 10-minute intervals. Scale bar, 20 µm. **(G)** Representative phase contrast image of SNU-475 cell with protrusions (green) segmented from superimposed contours used in morphodynamic analysis. Extension vectors (purple arrows) were drawn from the center of the cell nucleus towards individual protrusions and related to the direction of cell motion (black arrow). Scale bar, 20 µm. **(H)** Rose graphs show the percentage of extension vector directions in 30° cones, normalized to the directions of random and EGF-guided (directed) motions (0°; arrows) of WT, KO, ΔIFBD, and PST-treated WT (WT+PST) SNU-475 cells. *n* = 9752 extensions in 22 cells (WT random), 4167 extensions in 15 cells (WT directed), 8394 extensions in 19 cells (KO random), 5107 extensions in 15 cells (KO directed), 8362 extensions in 21 cells (ΔIFBD random), 5809 extensions in 19 cells (ΔIFBD directed), 9450 extensions in 20 cells (WT+PST random), 4350 extensions in 14 cells (WT+PST directed); *N* = 3. Bar graphs show the percentage of cell extensions formed either in the direction of motion (frontal, 30° to -30° cones) or along the rest of the cell perimeter (rest). Data are shown as mean ± SEM; dots, biological replicates; *N* = 3. Two-tailed *t*-test; *$P < 0.05$; **$P < 0.01$;† $P < 0.001$.

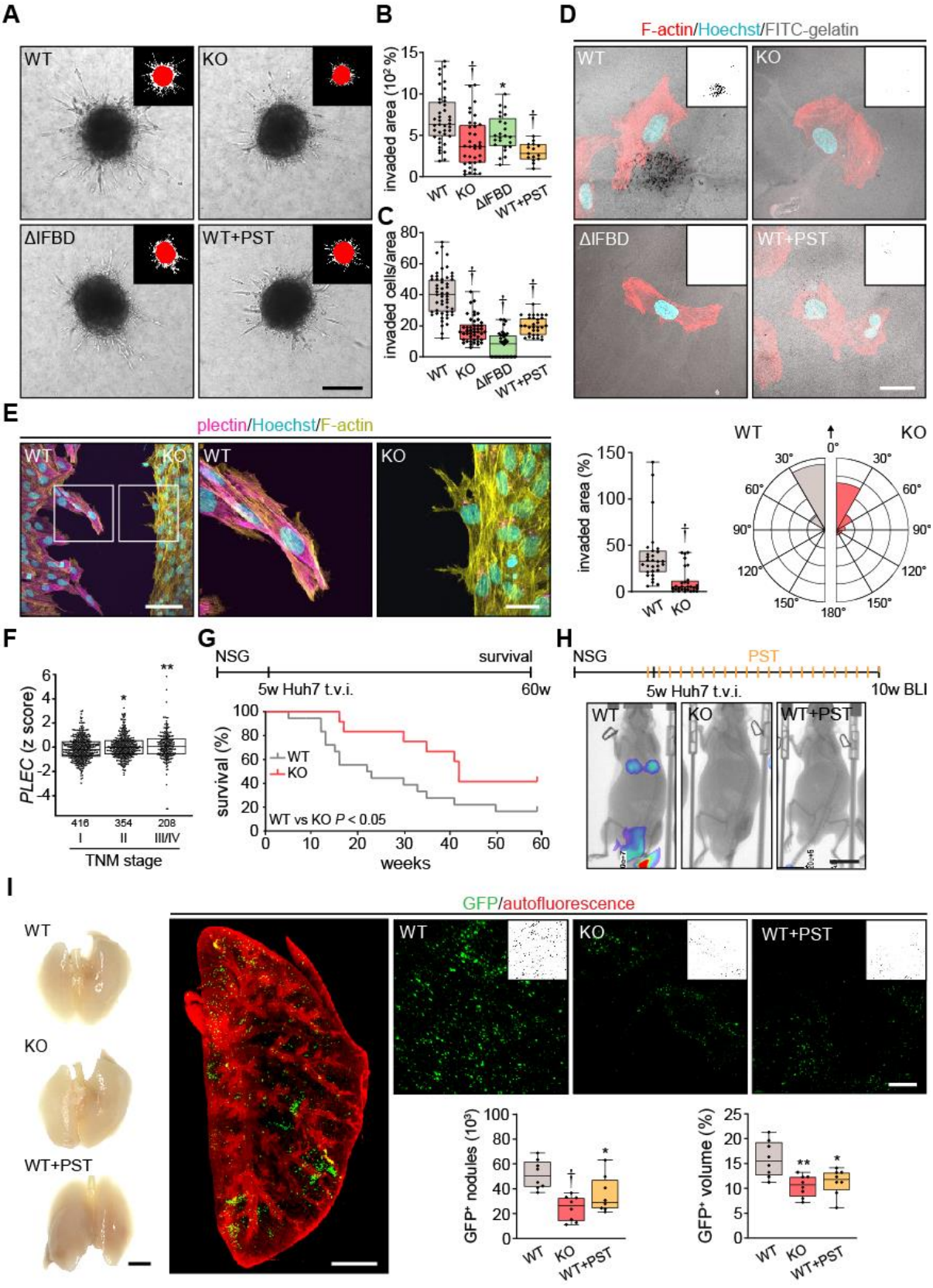

Figure 6. Plectin inactivation inhibits HCC invasion and metastasis. (A) Representative images of WT, KO, ΔIFBD, and PST-treated WT (WT+PST) SNU-475 spheroids grown for 3 days in collagen mixture. Insets, superimposed binary masks of initial (red) and final (white) spheroid area. Scale bar, 200 µm.

(B) Quantification of the invaded area calculated as the percentage of the initial spheroid area from day 0. Boxplots show the median, 25th, and 75th percentile with whiskers reaching the last data point; dots, individual spheroids; *n* = 47 (WT), 44 (KO), 34 (ΔIFBD), 25 (WT+PST) spheroids; *N* = 5 (WT, KO), 4 (ΔIFBD), 3 (WT+PST). Two-tailed *t*-test; ***P* < 0.01; †*P* < 0.001. **(C)** Quantification of the number of indicated cells invaded in Matrigel transwell assay. Boxplots show the median, 25th, and 75th percentile with whiskers reaching the last data point; dots, fields of view; *n* = 51 (WT), 45 (KO), 38 (ΔIFBD), 31 (WT+PST) fields of view; *N* = 4 (WT, KO), 3 (ΔIFBD, WT+PST). Two-tailed *t*-test; †*P* < 0.001. **(D)** Representative confocal micrographs of WT, KO, ΔIFBD, and PST-treated WT (WT+PST) SNU-475 cells grown on FITC-labeled gelatin (grey) for 24 hours and stained for F-actin (red). Nuclei, Hoechst (blue). Insets, segmented binary masks of FITC-gelatin signal. Black regions correspond to gelatin areas degraded by individual cells. Scale bar, 30 µm. **(E)** Representative confocal images of WT and KO SNU-475 cells during the Matrigel invasion assay, stained for plectin (magenta) and F-actin (yellow). Nuclei, Hoechst (blue). See Video 1. Boxed areas, x3 images. Scale bars, 100 and 30 µm (boxed areas). Boxplot shows the invaded area calculated as the percentage of the initial area covered by WT and KO cells. The box represents the median, 25th, and 75th percentile with whiskers reaching the last data point; dots, fields of view; *n* = 29 fields of view; *N* = 2. Rose graphs show the percentage of extension vector directions in 30° cones, normalized to the directions of cell motions (0°; arrow) during matrigel invasion. *n* = 857 extensions in 18 cells (WT), 623 extensions in 12 cells (KO); *N* = 2. Two-tailed *t*-test; †*P* < 0.001. **(F)** Relative *plectin* (*PLEC*) mRNA expression in samples collected from HCC patient meta-cohort clustered based on TNM classification (stage I-IV). The meta-cohort includes 6 different datasets from 5 platforms (for details, see Materials and methods section). The numbers of participants per stage are indicated in the graph. Scattered boxplots show individual data points, median, 25th, and 75th percentile; *N* = 978. Wilcoxon rank-sum test; **P* < 0.05; ***P* < 0.01. **(G)** The 5-week-old NSG mice were injected (t.v.i.) with WT and KO RedFLuc-GFP-expressing Huh7 cells generated for lung colonization assay. Kaplan-Meier curves show the overall survival of mice injected with the cells indicated. *N* = 14 (WT), 13 (KO). Long-rank test, *P* < 0.05. **(H)** The 5-week-old NSG mice were injected (t.v.i.) with indicated RedFLuc-GFP-expressing Huh7 cells. WT cell-bearing mice were kept either untreated or every second day provided with orogastric gavage of plecstatin (WT+PST) as indicated. Five weeks post-injection mice were screened by whole-body bioluminescence imaging (BLI). Representative BLI images of WT, KO, and PST-treated WT (WT+PST) Huh7 cells-bearing mice are shown. Scale bar, 2 cm. **(I)** Representative images of lungs dissected from mice shown in (H). Scale bar, 1 cm. Representative lattice light sheet fluorescence image of clear, unobstructed brain imaging cocktails (CUBIC)-cleared lung lobe immunolabeled with antibodies against GFP (green). Autofluorescence visualizing the lobe structures is shown in red. Scale bar, 2 mm. Representative

magnified images from lung lobes with GFP-positive WT, KO, and WT+PST Huh7 nodules. Insets, segmented binary masks of GFP-positive metastatic nodules. Scale bar, 400 µm. Boxplots show metastatic load in the lungs expressed as the number (left graph) and relative volume (right graph) of indicated GFP-positive (GFP^+) nodules. The box represents the median, 25th, and 75th percentile with whiskers reaching the last data point; dots, lung lobes; n = 8 lung lobes; N = 4. Two-tailed t-test; *P < 0.05; **P < 0.01; †P < 0.001.

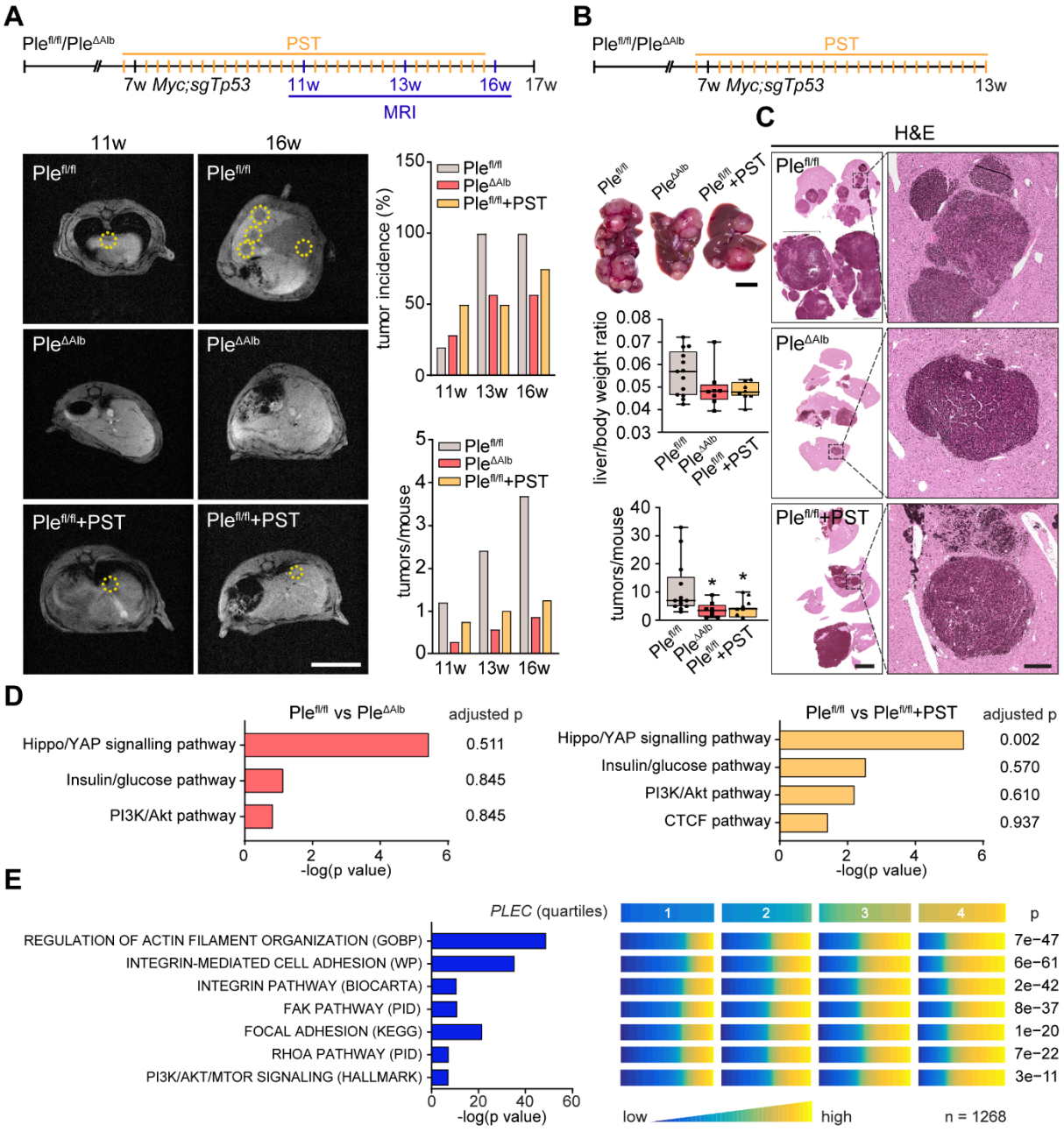

Figure 7. Genetic and pharmacological plectin targeting prevents hepatocarcinogenesis through signatures shared by animal models and patients. (A) HCC-predisposing lesions were introduced by hydrodynamic gene delivery via tail vein injection (HDTVi) of transposon vector encoding cMyc in conjunction with CRISPR/Cas9 construct targeting *Tp53* (Myc;sgTp53) in *Ple*$^{fl/fl}$ and *Ple*$^{\Delta Alb}$ cohorts of 7-week-old male mice. *Ple*$^{fl/fl}$ mice were kept either untreated or every second day provided with orogastric gavage of plecstatin (*Ple*$^{fl/fl}$+PST) and the development of HCC was monitored by MRI at 11, 13, and 16 week, as indicated. Representative MRI images of *Ple*$^{fl/fl}$ and *Ple*$^{\Delta Alb}$ and *Ple*$^{fl/fl}$+PST tumors acquired at indicated time points. Dashed circles, tumors. Scale bar, 2 cm. Graphs show the average number of tumors (lower graph) and percentual tumor incidence (upper graph) inferred from MRI

images. *N* = 5 (*Ple*$^{fl/fl}$), 7 (*Ple*$^{\Delta Alb}$), 4 (*Ple*$^{fl/fl}$+PST). **(B)** Myc;sgTp53 HCC was induced in *Ple*$^{fl/fl}$, *Ple*$^{\Delta Alb}$, and PST-treated *Ple*$^{fl/fl}$ (*Ple*$^{fl/fl}$+PST) male mice as in (A). Shown are representative images of *Ple*$^{fl/fl}$, *Ple*$^{\Delta Alb}$, and *Ple*$^{fl/fl}$+PST livers from mice with fully developed multifocal HCC sacrificed 6 weeks post-induction. Scale bar, 1 cm. Boxplots show tumor burden in the livers expressed as the liver/body weight ratio (upper graph) and number of tumors per mouse (lower graph). The box represents the median, 25th, and 75th percentile with whiskers reaching the last data point; dots, mice; *N* = 12 (*Ple*$^{fl/fl}$), 9 (*Ple*$^{\Delta Alb}$), 10 (*Ple*$^{fl/fl}$+PST). Two-tailed *t*-test; **P* < 0.05. **(C)** Representative images of H&E-stained *Ple*$^{fl/fl}$, *Ple*$^{\Delta alb}$, and *Ple*$^{fl/fl}$+PST liver sections. Note darker areas corresponding to HCC lesions. Boxed areas, x12 images. Scale bars, 5 and 1 mm (boxed areas). **(D)** Gene set enrichment analysis of differentially regulated proteins in *Ple*$^{fl/fl}$ vs *Ple*$^{\Delta Alb}$ and *Ple*$^{fl/fl}$ vs *Ple*$^{fl/fl}$ + PST livers from the cohort shown in (A). Prediction of canonical signaling pathways in *Ple*$^{fl/fl}$ vs *Ple*$^{\Delta Alb}$ (left) and *Ple*$^{fl/fl}$ vs *Ple*$^{fl/fl}$ + PST (right) proteomes. **(E)** Association of plectin-dependent signatures compiled from human HCC-derived cells (see Fig. 3B-E) and mouse models (see Fig. 7D) with *plectin* (*PLEC*) mRNA expression in HCC patients. Right panel shows the levels of selected signatures in patients grouped into quartiles of *PLEC* expression level. *N* = 1268. *P* values were generated from an analysis of variance (ANOVA).